# Synaptotagmin 7 outperforms synaptotagmin 1 to open and stabilize nascent fusion pores via robust membrane penetration

Kevin C. Courtney[1], Taraknath Mandal[2,3], Yueqi Li[1,4], Nikunj Mehta[1], Debasis Das[1,5], Qiang Cui[2] and Edwin R. Chapman[1†]

[1] Howard Hughes Medical Institute and the Department of Neuroscience, University of Wisconsin, 1111 Highland Avenue, Madison, Wisconsin, 53705
[2] Department of Chemistry, Boston University, Boston, MA, 02215
[3] Department of Physics, Indian Institute of Technology – Kanpur, Kanpur 208016, India
[4] Center for Bioanalytical Chemistry, University of Science and Technology of China, Hefei, 230026, China
[5] Department of Biological Sciences, Tata Institute of Fundamental Research, Homi Bhabha Road, Navy Nagar, Colaba, Mumbai - 400005, India.

[†]Corresponding author: E-mail: chapman@wisc.edu

## Abstract

$Ca^{2+}$-triggered exocytosis is a crucial aspect of neuronal and neuroendocrine cell function, yet many of the underlying molecular mechanisms that regulate these processes are unknown. Here, we contrast the biophysical properties of two prominent neuronal $Ca^{2+}$ sensors, synaptotagmin (syt) 1 and syt7. In both proteins, four $Ca^{2+}$-binding loops partially penetrate bilayers that harbor anionic phospholipids, and mutagenesis studies suggest that these interactions are important for function. However, these mutations also alter the interaction of syts with the SNARE proteins that directly catalyze membrane fusion. To directly assess the role of syt membrane penetration, we took a different approach and found that $Ca^{2+}$-syt1-membrane interactions are strongly influenced by membrane order; tight lateral packing of phosphatidylserine abrogates syt1 binding to lipid bilayers due to impaired membrane penetration. Function could be restored by making the membrane penetration loops more hydrophobic, or by inclusion of cholesterol. In sharp contrast, syt7 unexpectedly exhibited robust membrane binding and penetration activity, regardless of the lipid acyl chain structure. Thus, syt7 is a 'super-penetrator'. We exploited these observations to specifically isolate and examine the role of membrane penetration in syt function. By altering bilayer composition, rather than protein structure, we disentangled the roles of syt-membrane versus syt-SNARE interactions. Using nanodisc-black lipid membrane electrophysiology, we demonstrate that membrane penetration underlies the ability of syts to directly regulate reconstituted, exocytic fusion pores in response to $Ca^{2+}$.

## Introduction

Within the seventeen-member family of mammalian synaptotagmin (syt) isoforms (1), syt1 and syt7 are currently the most heavily studied (2, 3). It is now established that both isoforms play important roles in the synaptic vesicle (SV) cycle and neurotransmission, but their detailed mechanisms of action remain unclear. Both isoforms bind $Ca^{2+}$ ions via each of their tandem C2-domains, designated C2A and C2B. Syt1 binds $Ca^{2+}$ with lower affinity (4), and responds to changes in [$Ca^{2+}$] with faster kinetics than syt7 (5). Syt1 is localized to SVs (2, 6-8), where it clamps spontaneous release (9, 10) under resting conditions. Then, upon depolarization and $Ca^{2+}$ entry (11, 12), syt1 functions to trigger and synchronize evoked release (9, 13-15). Syt1 also has additional functions, including the formation of the readily releasable pool of SVs (16), SV docking (17), and the kinetics of endocytosis (18, 19). In contrast, syt7 resides on the axonal plasma membrane (20, 21) in nerve terminals where it supports asynchronous neurotransmitter release (22, 23). Additionally, syt7 KOs exhibit alterations in short term synaptic plasticity, including a loss of paired pulse facilitation (24) and enhanced synaptic depression with impaired SV replenishment (25), without affecting spontaneous or single-stimulus evoked neurotransmitter release (25, 26). Recently, syt7 was shown to promote activity-dependent docking of SVs at active zones (21, 23), which may provide a unifying mechanism to support the multitude of functions described for this isoform. Notably, this syt7 docking function was determined to be upstream of Doc2α, a $Ca^{2+}$ sensor for asynchronous neurotransmitter release (23, 27). In addition to being targeted to the plasma membrane of axons, syt7 also resides on the surface of lysosomes (28) to promote plasma membrane repair (29). Furthermore, both syt1 and syt7 are present on dense core vesicles in neurons and in chromaffin cells where they are thought to serve as $Ca^{2+}$ sensors for exocytosis (30-32). Whether syt7 is present on the secretory vesicle or the plasma membrane might confer unique functional roles in exocytosis.

Although there is a long history of *in vitro* reconstitution and functional characterization (33) of syt1, to date, the successful purification of full-length syt7 has not been reported. This has precluded direct comparisons between full-length versions of these isoforms in reduced systems. With respect to their molecular mechanisms, there is a consensus that upon binding $Ca^{2+}$, the C2-domains syt1 and syt7 partially penetrate membranes the harbor anionic phospholipids (34, 35). This membrane penetration step might serve to destabilize the local phospholipid environment by introducing volume into the bilayer, buckling the membrane, and lowering the energy barrier for fusion (34, 36-39). Additionally, membrane penetration could stabilize curved intermediate structures (40). Finally, since syt1 and 7 are membrane-anchored proteins, interactions between their C2-domains and 'target' membranes serves to closely juxtapose the bilayers that are destined to fuse, thus facilitating SNARE-mediated fusion.

The importance of syt1 membrane penetration is supported by *in vitro* mutagenesis studies. In each C2-domain, the distal tips of two $Ca^{2+}$ binding loops insert into membranes upon binding $Ca^{2+}$ (33, 34, 41). Substitution of residues at the tips of these loops, with four tryptophan residues (4W) to increase hydrophobicity, enhances membrane binding and bending, while substitution with alanines (4A) reduces membrane association (39, 42). Moreover, when these mutant proteins are expressed in syt1 KO neurons, 4A fails to rescue synchronous neurotransmitter release whereas 4W expression exhibits a significant increase in

EPSC amplitude and $Ca^{2+}$-sensitivity, compared to WT syt1 (43, 44). However, the 4W and 4A mutations have other effects on syt1 biochemistry, including altered interactions with SNARE proteins (39). Additional approaches are needed to unambiguously define the precise role of syt1-membrane interactions in fusion.

Here, we examine how membrane binding and penetration by the C2-domains of syt1 and syt7 contribute to $Ca^{2+}$-triggered membrane fusion. Specifically, we use phospholipid bilayer order as a tool to explore the link between $Ca^{2+}$-syt membrane penetration and the regulation of reconstituted fusion pores, which represents the first crucial intermediate in the fusion reaction. We demonstrate that syt function can be controlled by manipulating PS acyl chain structure. In particular, syt1 cannot bind or penetrate into bilayers containing phosphatidylserine that has saturated acyl chains; without efficient membrane penetration, syt1 fails to respond to $Ca^{2+}$ to regulate fusion pores. Interestingly, we observed that syt7 displays far more robust membrane penetration activity as compared to syt1, and efficiently penetrated all bilayers that were tested, regardless of the membrane order. Furthermore, we report the first use and characterization of reconstituted full-length syt7 and determine, via comparisons with syt1, that the ability of C2-domains to penetrate membranes underlies how of these proteins to regulate fusion pores.

## Results

### Syt7, but not syt1, penetrates membranes that harbor saturated PS

To compare how syt1 and syt7 interact with phospholipid bilayers, we first performed a well-described syt-loop penetration assay (34, 45). For this, we labeled the cytoplasmic domains (denoted C2AB) of each isoform with a solvatochromic fluorescent dye, NBD, on a cysteine residue placed in the distal tip of a membrane penetration loop (loop-3) in C2B. In the absence of $Ca^{2+}$ (EGTA), the C2AB domains do not interact appreciably with 100 nm PC/PS (80:20) liposomes, resulting in a low fluorescence signal (**Figure 1A-C**). Upon binding $Ca^{2+}$, the C2AB domains rapidly associate with the membrane and partially insert into the hydrophobic core of the bilayer (34, 35), causing a significant increase in blue-shifted NBD fluorescence (**Figure 1A-C**). To specifically examine the contribution of hydrophobic interactions to the binding reaction, we compared the ability of syt1 and syt7 to penetrate into bilayers containing 20% PS with either saturated (16:0/16:0) or unsaturated acyl chains (18:1/18:1), also notated as dipalmitate-phosphatidylserine (DPPS) and dioleate-phosphatidylserine (DOPS), respectively; the remaining 80% of the lipids in both conditions were unsaturated dioleate-phosphatidylcholine (DOPC) (**Figure S1)**. Knowing that syt1 and syt7 are PS binding proteins, we postulated that tight lateral packing of saturated PS acyl chains in the liposomes might render the bilayers refractory to penetration, thus restricting hydrophobic interactions. As expected, syt1 and syt7 were both able to penetrate bilayers containing unsaturated DOPS (**Figure 1B & 1C**). However, if the PS acyl chains are fully saturated, syt1 C2AB penetration was significantly reduced (**Figure 1B**), despite having 80% of the bilayer composed of unsaturated DOPC. Surprisingly, we found syt7 exhibited comparable penetration into saturated and unsaturated PS bilayers (**Figure 1C**), indicating a more robust mode of binding.

To establish the generality of the syt1 penetration defect into saturated PS-bilayers, we examined the membrane penetration performance of other C2-domain-containing proteins

under the same conditions as were used with syt1 and syt7. We engineered a single cysteine substitution into the third loop of the C2-domains from protein kinase C (PKC) and cytosolic phospholipase A2 (cPLA2), as well as the third loop in the C2B domain of Doc2β C2AB. We found that all three proteins also displayed significantly impaired penetration into membranes with saturated acyl chains in response to $Ca^{2+}$ (**Figure S2**), thus the robust penetration of syt7 into DPPS bilayers appears unique.

**Molecular dynamics simulations show saturated PS clusters resist syt1 C2B-domain penetration**

Next, to further examine how syt1 and syt7 interact with bilayers containing saturated and unsaturated PS, we conducted all-atom molecular dynamics (MD) simulations of their C2B domains with phospholipid bilayers, again using the same lipid compositions used above. We first performed lipid-only MD simulations to monitor the stability of DOPS and DPPS clusters in the DOPC/DxPS (80:20) bilayers. We postulated that DPPS may form a tight cluster, thus restricting C2-domain penetration. For this initial test, a small cluster of 32 PS lipids, either DOPS or DPPS, was placed in the center of a DOPC membrane (**Figure S3A**) and equilibrated for 450 ns using MD simulations. **Figure 2A** shows that DPPS lipids (cyan) are much more compact than DOPS lipids (blue), suggesting that the saturated PS lipids are likely to form bigger, more stable clusters in a saturated-unsaturated lipid mixture (**Supplemental movies 1 & 2**). We then quantified how clustered the two PS species were at the end of the simulations by measuring the midpoint distances between the PS molecules; the radial distribution function (RDF), shows that the DPPS molecules remain in close proximity with a peak centered around 0.75 nm. In contrast, the DOPS molecules are more dispersed, as indicated by a shorter peak height with a broad distribution (**Figure 2B**). These initial MD simulations were also validated via atomic force microscopy (AFM) imaging of supported lipid bilayers containing DOPS or DPPS; we found that $Ca^{2+}$ reversibly caused DPPS to segregate into 15 ± 7 nm clusters in the bilayer (**Figure S4A**). In contrast, no lipid clustering was observed in the DOPS condition (**Figure S4B**).

We then carried out a second set of MD simulations to examine how PS acyl chain structure affects C2-domain-membrane interactions. The isolated C2B domain of syt1 (orange) or syt7 (yellow) was placed on top of the membrane such that the membrane penetration loops were positioned close to the PS cluster (**Figures S3B & S3C**). The system was solvated and charge neutralized by adding $Ca^{2+}$ and $Cl^-$ ions. Upon equilibration of the C2B domains, we found that $Ca^{2+}$-bound loops 1 and 3 of syt1 and syt7 spontaneously inserted into, and remained inside, the DOPC/DOPS membrane throughout the 1000 ns long MD simulations (**Figures 2C**). In both cases, the insertion depth of loop 3 was greater than the depth of loop 1, while loop 2 remained away from the lipid head groups (**Figures 2C,** *lower panel*). Insertion of loops 1 and 3 allows the hydrophobic residues, V304 and I367 of syt1, and I298 and L361 of syt7, to access the hydrophobic bilayer core, strengthening the binding interaction. This result matches well with previous experimental results from our laboratory (45). In contrast to the syt1-DOPS simulation, tight packing of the PS lipids in the DOPC/DPPS membrane does not allow strong binding or insertion of the syt1 C2B domain (**Figure 2D**, *left panel*). However, in line with our experimental results (**Figure 1C**), we found that the syt7 C2B loops penetrated well into the DPPS cluster (**Figure 2D**, *right panel*).

**Cholesterol rescues the syt1 membrane penetration defect**

The experiments and MD simulations above reveal that acyl chain packing strongly affects the ability of syt1, but not syt7, to penetrate membranes in response to $Ca^{2+}$. We therefore tested whether 'loosening' this lateral packing can rescue syt1 function using bilayers that harbored DPPS. Physiological lipid bilayers contain approximately 30 - 40% cholesterol (6, 46). Cholesterol displays unique membrane modulating properties by reducing the rotational mobility (stiffening) of unsaturated acyl chains, while also adding space between (loosening) tightly packed saturated acyl chains. We therefore hypothesized that introducing cholesterol into the DPPS bilayer would loosen the PS clusters and allow the syt1 C2B domain to penetrate the otherwise refractory membrane. After repeating the DPPS MD simulations in the presence of 30% cholesterol, we indeed found that loops 1 and 3 of syt1 C2B could again penetrate the DPPS membrane (**Figure 3A & 3B**). Correspondingly, in AFM experiments, $Ca^{2+}$ failed to induce detectable clusters in DPPS supported lipid bilayers that contained 30% cholesterol (**Figure S4C**).

Next, we revisited the syt1 NBD-loop penetration experiments described in **Figure 1** to further examine the effects of cholesterol, experimentally. First, we used soluble cholesterol-loaded methyl-β-cyclodextrin (sChol) to introduce cholesterol into DOPC/DPPS bilayers while monitoring changes in NBD fluorescence in real-time (**Figure 3C**). As described above (**Figure 1B**), $Ca^{2+}$-bound syt1 C2AB can only minimally penetrate DPPS-containing bilayers, as indicated by a relatively low fluorescence signal under this condition (**Figure 3D**, grey trace). However, after of the addition of sChol, to incorporate cholesterol into the liposomes, syt1 C2AB regained the ability to penetrate the bilayer (**Figure 3D,** black trace), showing maximal penetration after approximately 10 minutes. This penetration rescue was also directly visualized in by microscopy of DOPC/DPPS giant unilamellar vesicles (GUVs) with and without 30% cholesterol (**Figure 3E**). No NBD fluorescence was observed on the GUV surface in the absence of $Ca^{2+}$; upon addition of $Ca^{2+}$, syt1 C2AB became associated with the cholesterol containing GUVs, as indicated by the appearance of the NBD signal on the outer membrane surface. Notably, the DOPC/DPPS GUVs without cholesterol fail to show any NBD signal on the GUV surface in response to $Ca^{2+}$ (**Figure 3E**).

We then generated DOPC/DPPS liposomes with increasing amounts of cholesterol, up to 30%, while monitoring membrane penetration by fluorometery. As with the real-time addition of cholesterol, discrete increases in the cholesterol concentration allowed syt1 C2AB to penetrate membranes, with an $EC_{50}$ of 17.6%, reaching maximal membrane penetration at 30% cholesterol (**Figure 3F**). Without cholesterol, approximately ten-fold more lipid to was needed to drive maximal penetration of syt1 C2AB into liposomes bearing DPPS (protein:lipid, 1:4000), compared to DOPS (protein:lipid, 1:400) (**Figure 3G**). However, if cholesterol is present, syt1 penetration is comparable for all PS species, across a wide range of protein/lipid ratios (**Figure 3G**). This effect of cholesterol on syt1 binding to DPPS rationalizes how Kiessling *et al.* (2018) observed syt1 triggering membrane fusion using bilayers containing saturated PS, as these membranes also contained 20% cholesterol (47). Together, these results support the conclusion that syt1 fails to penetrate DPPS-containing membranes, due to the rigidity of the bilayer.

However, the attributes of syt7 that enabled robust penetration into DPPS bilayers remained unclear; this is addressed further below.

**C2-domain binding to phospholipid bilayers is coupled with membrane penetration**

To determine whether the compromised membrane penetration of syt1 was also accompanied by a failure to bind electrostatically to the liposome surface, we performed a protein-liposome co-sedimentation assay. The C2AB domains were mixed with 100 nm liposomes that were composed of 20% saturated (DPPS) or unsaturated PS (DOPS), in 0.2 mM EGTA or 0.5 mM free $Ca^{2+}$, followed by ultracentrifugation to pellet the liposomes (**Figure 4A**); bound proteins co-sediment with the liposomes. C2AB domains from both syt1 and syt7 efficiently bound DOPS-containing liposomes in the presence of $Ca^{2+}$, as indicated by a depletion of protein from the supernatant (**Figure 4B**). However, analogous to the penetration data, only 20-25% of syt1 C2AB bound DPPS-bearing liposomes in $Ca^{2+}$ (**Figure 4C**). This validates that membrane insertion is a prerequisite for syt1-membrane binding, presumably by providing hydrophobic interactions; electrostatic interactions are apparently insufficient to enable syt1 binding in isolation. This conclusion is consistent with earlier mutagenesis studies (39) In contrast to syt1, and in agreement with the penetration results, we found that syt7 maintained robust binding to liposomes bearing either unsaturated or saturated PS (**Figure 4B & 4C**), further supporting the idea that membrane binding is coupled with penetration. Notably, we consistently observed that approximately 25-30% of the syt7 bound to the liposomes in EGTA; this might reflect the propensity of DPPS to form clusters, thereby increasing the local concentration of this lipid. Indeed, a previous report showed that syt7 exhibits robust $Ca^{2+}$-independent binding to liposomes, as a function of the mole fraction of PS (48).

**Hydrophobic residues are critical for C2-domain membrane binding**

The membrane binding and penetration assays described above revealed that the C2-domains of syt1 and syt7 engage distinctly with lipid bilayers. We therefore compared the amino acid sequences of their membrane penetration loops; overall, the sequences are highly conserved (**Figure 4D**). The most notable differences are that the syt1 loops contain three more hydrophobic residues, and three fewer positive charged residues (excluding the histidine residues in the syt1 loops at physiological pH) than the syt7 loops. This could be expected to equip syt1 with comparatively enhanced penetration activity, and syt7 with prominent electrostatic binding component; instead, we found that syt7 displayed enhanced membrane binding (**Figure 4B & 4C**) and penetration (**Figure 1C**). To delve into this further, we generated a series of mutants to examine how the hydrophobic and cationic character of the loops influenced binding. These included a syt1 C2AB construct that contained five tryptophan substitutions in the penetration loops (syt1 5W) to increase hydrophobicity, or a poly-cationic mutant (L171K, H198K, K236R, N333R, Y364K, K369R) that substituted all the cationic residues of the syt7 loops on to syt1 (syt1 s7+). Note that while K236R and K369R in the syt1 s7+ construct do not affect the charge at these two positions, arginine residues have been reported to exhibit enhanced interfacial binding to phospholipids, compared to lysines (49). We

also examined a syt7 C2AB mutant with reduced hydrophobicity (F167, F229, I298, L361A) in the penetration loops (syt7 4A).

We first tested how syt1 5W, syt1 s7+ and syt7 4A performed against the refractory bilayers containing saturated DPPS. Co-sedimentation assays revealed that syt1 5W was indeed able to enhance membrane binding in response to $Ca^{2+}$; the tryptophan substitution enabled syt1 5W to bind equally well to DOPS and DPPS (**Figure 4E & 4F**). Moreover, NBD-labelled syt1 5W was able to penetrate efficiently into DPPS bilayers (**Figure S5**). In contrast, the syt1 s7+ construct did not improve binding to DPPS in response to $Ca^{2+}$ (**Figure 4E & 4F**). In fact, syt1 s7+ also displayed a partial reduction in binding to DOPS in $Ca^{2+}$; in short, this mutant exhibited the opposite of the predicted effect. When examining syt7 4A, we found this construct had a reduced ability to bind DPPS in $Ca^{2+}$, compared to WT syt7 (**Figure 4C, 4E & 4F**), again highlighting the importance of hydrophobic residues in the loops.

To further explore how electrostatic interactions contribute to syt-membrane interactions, we conducted protein-liposome co-sedimentation experiments as a function of increasing ionic strength. We observed that syt1-membrane binding was highly sensitive to the salt concentration, whereas WT syt7 was entirely resistant (**Figure 4G & 4H**), as reported previously (34, 45, 50). We then repeated these experiments using syt1 5W, syt1 s7+ and syt7 4A. We found that increasing the hydrophobicity of syt1 (syt1 5W) had a greater impact on overcoming salt sensitivity, compared with positive charged residue substitutions (**Figure 4G & 4H**); bestowing the electrostatics of syt7 loops onto syt1 (syt1 s7+) did not improve salt resistance. This syt1 s7+ result is surprising considering this construct contains prominent hydrophobic and electrostatic character yet is still outperformed by WT syt7. Moreover, syt1 5W was also outperformed by WT syt7 in this assay. In line with the DPPS co-sedimentation experiments (**Figure 4E & 4F**), we also observed that hydrophobicity is critical for salt-insensitivity of syt7, as the 4A mutation enabled modest increases in salt (200 mM) to disrupt binding (**Figure 4G & 4H**). To tease apart contributions of each syt7 C2-domain, we generated and tested syt7 C2AB constructs with reduced loop hydrophobicity in either the C2A (syt7 $C2A_{2A}B$) domain or the C2B (syt7 $C2AB_{2A}$) domain. These results demonstrated that the C2A domain of syt7 is responsible for the salt insensitivity, whereas the syt7 $C2AB_{2A}$ mutation had no effect (**Figure 4G & 4H**). We also found, via stopped-flow rapid mixing experiments, that the membrane dissociation kinetics of each of these constructs shared the same trends as the co-sedimentation studies (**Figure 4I**). Specifically, the 5W mutation slowed syt1 dissociation from liposomes and both the syt7 4A and syt7 $C2A_{2A}B$ mutations dramatically increased the dissociation rate (**Figure 4I**), further supporting the importance of loop hydrophobicity. Curiously, we found that the syt7 $C2AB_{2A}$ mutation reproducibly slowed the dissociation kinetics (**Figure 4I**). At present, a mechanism for this perplexing $C2AB_{2A}$ mutation effect is unknown.

Our data support previous conclusions (39, 43) that C2-domain loop hydrophobicity is critical for membrane binding, especially when contrasting our syt7 4A and syt1 s7+ results (**Figure 4E & 4F**). However, considering syt7 has higher membrane binding affinity (**Figure S6**), with fewer hydrophobic residues in the loops, compared to syt1 (**Figure 4D**), these results highlight the somewhat counterintuitive complexity of C2-domain-membrane interactions, which cannot easily be predicted from the primary sequence. These results indicate that the hydrophobicity of the C2-domain loops may be more important than the cationic properties in

governing membrane binding. However, additional factors, other than the sum of hydrophobic and electrostatic residues in the loops, appear to influence C2AB-membrane interactions.

**Membrane penetration is required for synaptotagmin 1 to dilate and stabilize fusion pores**

Having established that PS acyl chain order can govern how C2-domains interact with lipid bilayers, we proceeded to investigate functional consequences of restricting syt membrane penetration. We reasoned that PS acyl chain structure could be exploited to specifically interrogate the relationship between membrane penetration and syt-mediated fusion pore expansion (51). For this, we used the recently developed nanodisc-black lipid membrane (ND-BLM) planar lipid bilayer electrophysiology approach (51, 52). Previously, we reported that 13 nm nanodiscs (ND) with three copies of the SV SNARE, synaptobrevin 2, ($ND_3$) make small unstable fusion pores (40, 52) in BLMs containing the t-SNAREs syntaxin-1a and SNAP-25. However, incorporation of syt1 into these NDs caused the fusion pores to expand into larger, more stable structures in response to $Ca^{2+}$ (51). This experimental system is, therefore, ideal to examine the direct role of syt1 in fusion pore formation and expansion/dilation. By substituting PS species within the BLM, we can examine how syt membrane penetration influences pore kinetic properties and dilation.

Classically, BLM experiments are conducted by first dissolving a lipid mixture in a solvent, such as n-decane, followed by using a fine tipped brush or glass capillary to paint the lipids across a small aperture to form a planar lipid bilayer (51). We found the critical lipid in this study, DPPS, to be insoluble in n-decane, making the standard BLM protocol unusable. We therefore developed a new strategy to form a planar lipid bilayer across the aperture of a standard BLM cup that could accommodate all lipids used in this study (described in detail in the Methods section). This approach involves resuspending the lipids in pure water and then pipetting a droplet of lipid across the aperture of the BLM cup (**Figure 5A**). The cup is then placed into a vacuum desiccator to evaporate the water and form a lipid film. Buffer is then applied, and the lipids self-assemble to form a bilayer across the aperture. In contrast to other BLM protocols, this new strategy also has the advantage of allowing the incorporation of t-SNAREs directly into the BLM lipid mixture, rather than requiring a second step to donate the t-SNAREs into the BLM after formation, as was done previously (51). This drying method was successfully able to form t-SNARE-incorporated bilayers, enabling DPPS ND-BLM experiments.

In line with Das *et al*. (2020) we validated that in the absence of $Ca^{2+}$ (0.5 mM BAPTA), $ND_3$-syt1 formed small and unstable fusion pores in all conditions (**Figure 5B & 5C**). The addition of $Ca^{2+}$ caused a significant increase in the current passing through $ND_3$-syt1 fusion pores that form in the DOPS-containing BLM (**Figures 5B & 5C**), indicative of an increase in pore size. $Ca^{2+}$ significantly increased the fraction of time that the $ND_3$-syt1 pores remained in the open state in the DOPS-containing BLM (**Figure 5D**). The peak of the open dwell time distribution was also shifted to longer open times by >100-fold (**Figure 5E**). Interestingly, we found that $Ca^{2+}$ failed to trigger syt1-mediated fusion pore expansion in the DPPS-containing BLM (**Figure 5B-5E**), presumably due to impaired membrane insertion. Specifically, the current passing through $ND_3$-syt1 pores formed in the DPPS-containing BLM was unchanged by the addition of $Ca^{2+}$; the open dwell time and the fraction of time that pores remained in the open

state were also unaffected by $Ca^{2+}$. Together, these data suggest that syt1 must penetrate the target membrane in order to drive stable fusion pore opening and dilation.

**Synaptotagmin 7 robustly penetrates ordered PS bilayers to dilate and stabilize fusion pores**

To further correlate membrane penetration with fusion pore opening and dilation we aimed to purify and reconstitute full-length syt1 5W (FL-syt1 5W), and full-length syt7 (FL-syt7) into NDs to compare with the WT syt1 ND-BLM recordings, as the C2AB domains of syt1 5W and syt7 were able to efficiently bind (**Figure 4C & 4F**) and penetrate (**Figure 1, 2 & S5**) into DPPS-containing bilayers. However, to date, the use of recombinant FL-syt7 has not been reported, presumably due to difficulty in purification. We were able to express and purify functional FL-syt7, using high volumes of starting material and a stringent protocol, which enabled us to examine the impact of FL-syt7 on fusion pores, as compared to FL-syt1 and FL-syt1 5W. We reasoned that if syt1 5W and syt7 C2AB domains were able to penetrate saturated PS bilayers, and if penetration is indeed critical for regulating pores, then both FL-syt1 5W and FL-syt7 should be capable of opening and dilating fusion pores that form in a DPPS-bearing BLM, in response to $Ca^{2+}$. Indeed, increased hydrophobicity was previously shown to enhance fusion pore expansion in HeLa cells expressing flipped t-SNAREs (53) and in PC12 cells (54). In line with enhanced penetration performance, compared to WT syt1, we found that FL-syt1 5W and FL-syt7 reconstituted into $ND_3$ both yielded significant increases in fusion pore current in the presence of $Ca^{2+}$ (**Figure 5B & 5C**). The addition of $Ca^{2+}$ also significantly increased the fraction of time that $ND_3$-syt1 5W and $ND_3$-syt7 pores were in the open state (**Figure 5D**) and the open dwell time distribution shifted to approximately 10-fold longer open times (**Figure 5E**).

When examining the kinetics of fusion pore transitions in the presence of $Ca^{2+}$, we found that the closing rates for $ND_3$-syt1 fusion pores formed in the DPPS-BLM were significantly faster than for the DOPS condition (**Figure 5F**, *upper panel*); FL-syt1 failed to stabilize the fusion pore open state when membrane penetration was impaired. Moreover, the closing rates of the $ND_3$-syt1 fusion pores in the DPPS-containing BLM were also significantly faster than the penetration-competent $ND_3$-syt1 5W and $ND_3$-syt7 samples when $Ca^{2+}$ was present (**Figure 1, 5F & S5**), further supporting the conclusion that stabilization of the open state is likely a direct consequence of C2-domain penetration into the target BLM. Interestingly, while $Ca^{2+}$ enabled $ND_3$-syt1 to significantly increase the fusion pore opening rate in the DOPS BLM, we found no difference in the opening rates between $ND_3$-syt1, $ND_3$-syt1 5W and $ND_3$-syt7 in the DPPS condition (**Figure 5F**, *lower panel* & **Figure S7**). The discrepancy in opening rates between the penetration competent samples, $ND_3$-syt1 in DOPS, as well as $ND_3$-syt1 5W and $ND_3$-syt7 in DPPS, may suggest that C2-domain membrane penetration is preceded by SNARE zippering. Alternatively, the presence of DPPS at the fusion pore site may alter the conformation of the t-SNAREs (47) or increase the local rigidity of the phospholipid bilayer (55), to affect pore opening. Indeed, it was previously demonstrated that saturated acyl chains reduce SNARE-mediated fusion (56). It is also noteworthy that in the ND-BLM BAPTA conditions, PC and PS (80% and 20%, respectively) are expected to be uniformly distributed throughout the BLM (**Figure S4A**). Therefore, SNARE-alone fusion pores could form in a PS-independent manner (i.e., by forming a malleable, DOPC rich fusion pore) and are thus less affected by the acyl

chain structure of the PS constituent. However, in the DPPS BLM, $Ca^{2+}$ is expected to cause the syts to act at the site of, or adjacent to, a rigid PS cluster (**Figure 2 & S4A**), which may affect the kinetics of pore opening. Regardless, upon pore opening, the penetration competent syts act to restrict closure and drive fusion pore dilation.

## Discussion

During membrane fusion, discrete phospholipid bilayers are tethered and drawn together by proteins to overcome significant energy barriers and drive membrane merger. Recently, we described that an accessory protein, complexin, promotes SNARE-mediated membrane fusion by stabilizing these curved intermediate structures via insertion of a C-terminal amphipathic helix at the fusion pore site (40). Syt1 has also been suggested to promote fusion via membrane insertion (34, 37-39). However, with the multitude of functions assigned to syt1, precisely how this molecule synchronizes $Ca^{2+}$ influx into nerve terminals with the release of neurotransmitter remains unclear. In particular, the specific contribution of syt1 membrane penetration in triggering the fusion reaction has not been rigorously established. For example, syt1 is thought to inhibit SV exocytosis in the absence of $Ca^{2+}$ (a fusion clamp) by binding SNAREs and preventing complete zippering (9). In principle, $Ca^{2+}$ binding could drive synchronized SV exocytosis, simply by re-directing syt1 away from the *trans*-SNARE complex to release the fusion clamp and trigger fusion, making membrane penetration inconsequential. Previous studies have examined the role of syt1 membrane penetration by mutagenesis to increase or decrease the hydrophobicity of the C2-domain penetration loops (39, 53, 57). These studies support the importance of membrane penetration, but – as described above - these mutants may have unintended effects on protein function that confound conclusions.

To specifically assess the role of syt1 membrane penetration in the fusion reaction, we took an alternative approach by primarily working with WT proteins and then manipulating the composition of the target membrane to control syt1-membrane interactions. We found that syt1 cannot bind or penetrate into phospholipid bilayers containing saturated PS (**Figure 1-4**). We reasoned that this phenomenon could be exploited to isolate the role of membrane penetration from SNARE binding to gain detailed insights into how syt1 triggers fusion. We also found that other C2-domain containing proteins (i.e. cPLA2, PKC and Doc2β) failed to penetrate into bilayers containing saturated acyl chains (**Figure S2**), which could be explored in future studies. Surprisingly, however, we discovered that syt7 exhibited robust membrane penetration into bilayers containing either saturated or unsaturated PS (**Figure 1 & 2**). This distinction enabled direct comparisons between syt1 and syt7, to tease apart the specific role of membrane penetration in syt function.

The distinct membrane penetration performance of syt1 and syt7, both experimentally (**Figure 1**) and via MD simulations (**Figure 2**), then led us to investigate a mechanism that enables syt7 to act as a 'super-penetrator'. We therefore examined the relative contributions of hydrophobic and electrostatic interactions in mediating syt-membrane binding. We demonstrate that $Ca^{2+}$-dependent binding of C2-domains to phospholipid bilayers requires membrane penetration (**Figure 4**); in isolation, electrostatic interactions are insufficient. Indeed, although $Ca^{2+}$-bound syt1 binds to di-acylated anionic lipids with high affinity, syt1 does not associate with mono-acylated PS (lyso-PS) (58), which originally suggested that syt1 membrane binding is

a combination of electrostatic and hydrophobic interactions. Hydrophobic residues in the membrane penetration loops of both syt1 and syt7 are indeed critical for maintaining binding to phospholipid bilayers (**Figure 4**). Specifically, increasing syt1 hydrophobicity overcomes the defect in binding to saturated PS and slows the membrane dissociation kinetics (**Figure 4E, 4F & 4I**), while reduced hydrophobicity renders syt7 susceptible to elevated salt (**Figure 4G & 4H**) and speeds up the dissociation kinetics (**Figure 4I**). Curiously, the primary amino acid sequence of the syt1 and syt7 penetration loops (**Figure 4D**) failed to predict the binding properties of these C2-domains, suggesting that membrane binding is more complex than simply a sum of their charged and hydrophobic residues.

After identifying that syt1 membrane binding can be controlled by manipulating the PS acyl chain structure, and that syt7 and a gain-of-function syt1 (syt1 5W) can overcome the saturated PS binding defect observed with WT syt1, we proceeded to test these three variants functionally using the ND-BLM approach. To our knowledge, this is the first reported purification and successful reconstitution of FL-syt7. We aimed to determine whether membrane penetration is required for syt1/7 to drive fusion pore opening and dilation. A new BLM method was developed in order to enable the formation of planar lipid bilayers containing all the lipids used in this study (**Figure 5A**). As predicted, we observed that stable fusion pore opening and dilation were directly correlated with the ability of syts to penetrate membranes. Specifically, when a C2-domain is incapable of penetrating into a bilayer, fusion pore stabilization and dilation were blocked. Conversely, conditions that permit the syts to penetrate membranes in response to $Ca^{2+}$ (syt1 into DOPS, or syt1 5W and syt7 into DPPS) result in larger, more stable fusion pores (**Figure 5**). This validates that syt membrane penetration directly mediates, at least in part, the regulation of fusion pores.

Kinetic analysis revealed that membrane penetration competent syts significantly reduced the fusion pore closing rates, thereby keeping pores in the open state for longer periods (**Figure 5F**). Notably, the ND-BLM system traps fusion pores in a reversible intermediate state, due to the rigid scaffold that surrounds the NDs. However, *in vivo*, no such restricting scaffold is present; the penetration action of the syts in neurons may instead favor a one-way reaction by stabilizing the nascent fusion pore, reducing the propensity to reverse towards closure, and supporting pore dilation. In this view, $Ca^{2+}$ binding by syts directs the C2-domains to penetrate into the target membrane, thus lowering the energy barrier for full fusion of SV with the plasma membrane.

It is interesting to note that, while syt7 was determined herein to exhibit more robust binding and penetration into lipid bilayers, as compared to syt1, recent findings suggest that syt7 does not act directly as a $Ca^{2+}$ sensor for SV exocytosis (21, 23). Instead syt7 functions as a dynamic, $Ca^{2+}$-regulated SV docking protein on the axonal plasma membrane that feeds vesicles to Doc2α during asynchronous neurotransmitter release (27). In this context, the extent to which syt7 membrane penetration contributes to SV exocytosis is unknown. Moreover, with highly curved ~42 nm SVs as the target membrane in this case, syt7 binding and penetration, to mediate SV docking, rather than fusion, may be the critical function. However, syt7 has also been reported to be a direct exocytic $Ca^{2+}$ sensor residing on lysosomes, contributing to lysosome-plasma membrane fusion (28) and on dense-core granules in chromaffin cells, to release neuropeptides (30). Yet another study suggested that syt7 on dense core vesicles plays a role in docking or priming, rather than fusion per se (32). Clearly, additional work is needed to

clarify the function of syt7, but an appealing idea is that syt7 functions differently when targeted to the presynaptic membrane versus when it is targeted to dense core vesicles or lysosomes.

In this study, we reconstituted FL-syt7 into NDs to facilitate a direct comparison with syt1 using the ND-BLM approach to assess whether it can directly modulate fusion pores, and if so, how membrane penetration influences this regulation. We established that syt7 exhibits unusually robust membrane binding properties and that membrane penetration is indeed a critical step that enables both syt1 and syt7 to directly regulate fusion pores in response to binding $Ca^{2+}$. We note that interrogation of syt1 and syt7 function in the ND-BLM experiment mimics, in a sense, dense-core granule exocytosis, due to both isoforms residing on the ND (i.e., the vesicle face). Ongoing studies will incorporate FL-syt7 into the BLM and syt1 in the ND to model SV biology, *in vitro,* with increased complexity. Moreover, with recombinant FL-syt7 readily in hand, future studies will use FL-syt7 to reconstitute the SV docking step, with the goal of developing an *in vitro* model to build a more complete understanding of the SV cycle.

**References**


1. A. C. Wolfes, C. Dean, The diversity of synaptotagmin isoforms. *Current Opinion in Neurobiology* **63**, 198-209 (2020).
2. N. Brose, A. G. Petrenko, T. C. Sudhof, R. Jahn, Synaptotagmin: a calcium sensor on the synaptic vesicle surface. *Science* **256**, 1021 (1992).
3. C. Li *et al.*, Ca2+-dependent and Ca2+-independent activities of neural and nonneural synaptotagmins. *Nature* **375**, 594-599 (1995).
4. A. Bhalla, W. C. Tucker, E. R. Chapman, Synaptotagmin isoforms couple distinct ranges of Ca2+, Ba2+, and Sr2+ concentration to SNARE-mediated membrane fusion. *Molecular Biology of the Cell* **16**, 4755-4764 (2005).
5. E. F. Hui *et al.*, Three distinct kinetic groupings of the synaptotagmin family: Candidate sensors for rapid and delayed exocytosis. *Proceedings of the National Academy of Sciences of the United States of America* **102**, 5210-5214 (2005).
6. S. Takamori *et al.*, Molecular anatomy of a trafficking organelle. *Cell* **127**, 831-846 (2006).
7. M. M. Bradberry *et al.*, Rapid and gentle immunopurification of brain synaptic vesicles. *Journal of Neuroscience* **42** (2022).
8. W. D. Matthew, L. Tsavaler, L. F. Reichardt, Identification of a synaptic vesicle-specific membrane-protein with a wide distribution in neuronal and neurosecretory tissue. *Journal of Cell Biology* **91**, 257-269 (1981).
9. J. D. Vevea, E. R. Chapman, Acute disruption of the synaptic vesicle membrane protein synaptotagmin 1 using knockoff in mouse hippocampal neurons. *Elife* **9**, 24 (2020).
10. J. T. Littleton, M. Stern, M. Perin, H. J. Bellen, Calcium dependence of neurotransmitter release and rate of spontaneous vesicle fusions are altered in Drosophila synaptotagmin mutants. *Proc Natl Acad Sci U S A* **91**, 10888-10892 (1994).
11. R. Miledi, Transmitter release induced by injection of calcium-ions into nerve terminals. *Proceedings of the Royal Society Series B-Biological Sciences* **183**, 421-425 (1973).
12. G. J. Augustine, How does calcium trigger neurotransmitter release? *Current Opinion in Neurobiology* **11**, 320-326 (2001).
13. E. R. Chapman, "How does synaptotagmin trigger neurotransmitter release?" in Annual Review of Biochemistry. (Annual Reviews, Palo Alto, 2008), vol. 77, pp. 615-641.
14. H. Bai *et al.*, Different states of synaptotagmin regulate evoked versus spontaneous release. *Nature Communications* **7**, 9 (2016).

15. M. Geppert *et al.*, Synaptotagmin-I - A major $Ca^{2+}$ sensor for transmitter release at a central synapse. *Cell* **79**, 717-727 (1994).
16. H. S. Liu, C. Dean, C. P. Arthur, M. Dong, E. R. Chapman, Autapses and Networks of Hippocampal Neurons Exhibit Distinct Synaptic Transmission Phenotypes in the Absence of Synaptotagmin I. *Journal of Neuroscience* **29**, 7395-7403 (2009).
17. N. E. Reist *et al.*, Morphologically docked synaptic vesicles are reduced in synaptotagmin mutants Drosophila. *Journal of Neuroscience* **18**, 7662-7673 (1998).
18. E. M. Jorgensen *et al.*, Defective recycling of synaptic vesicles in synaptotagmin mutants of Caenorhabditis elegans. *Nature* **378**, 196-199 (1995).
19. K. Nicholson-Tomishima, T. A. Ryan, Kinetic efficiency of endocytosis at mammalian CNS synapses requires synaptotagmin I. *Proceedings of the National Academy of Sciences of the United States of America* **101**, 16648-16652 (2004).
20. S. Sugita *et al.*, Synaptotagmin VII as a plasma membrane Ca2+ sensor in exocytosis. *Neuron* **30**, 459-473 (2001).
21. J. D. Vevea *et al.*, Synaptotagmin 7 is targeted to the axonal plasma membrane through γ-secretase processing to promote synaptic vesicle docking in mouse hippocampal neurons. *Elife* **10** (2021).
22. H. Wen *et al.*, Distinct roles for two synaptotagmin isoforms in synchronous and asynchronous transmitter release at zebrafish neuromuscular junction. *Proceedings of the National Academy of Sciences of the United States of America* **107**, 13906-13911 (2010).
23. Z. Wu *et al.*, Synaptotagmin 7 docks synaptic vesicles for Doc2α-triggered asynchronous neurotransmitter release. *bioRxiv*, 2022.2004.2021.489101 (2022).
24. S. L. Jackman, J. Turecek, J. E. Belinsky, W. G. Regehr, The calcium sensor synaptotagmin 7 is required for synaptic facilitation. *Nature* **529**, 88-+ (2016).
25. H. S. Liu *et al.*, Synaptotagmin 7 functions as a Ca2+-sensor for synaptic vesicle replenishment. *Elife* **3**, 18 (2014).
26. A. Maximov *et al.*, Genetic analysis of synaptotagmin-7 function in synaptic vesicle exocytosis. *Proceedings of the National Academy of Sciences of the United States of America* **105**, 3986-3991 (2008).
27. J. Yao, J. D. Gaffaney, S. E. Kwon, E. R. Chapman, Doc2 Is a Ca2+ Sensor Required for Asynchronous Neurotransmitter Release. *Cell* **147**, 666-677 (2011).
28. I. Martinez *et al.*, Synaptotagmin VII regulates Ca2+-dependent exocytosis of lysosomes in fibroblasts. *Journal of Cell Biology* **148**, 1141-1149 (2000).
29. A. Reddy, E. V. Caler, N. W. Andrews, Plasma membrane repair is mediated by Ca2+-regulated exocytosis of lysosomes. *Cell* **106**, 157-169 (2001).
30. M. Bendahmane *et al.*, Synaptotagmin-7 enhances calcium-sensing of chromaffin cell granules and slows discharge of granule cargos. *Journal of Neurochemistry* **154**, 598-617 (2020).
31. J. S. Schonn, A. Maximov, Y. Lao, T. C. Sudhof, J. B. Sorensen, Synaptotagmin-1 and-7 are functionally overlapping Ca2+ sensors for exocytosis in adrenal chromaffin cells. *Proceedings of the National Academy of Sciences of the United States of America* **105**, 3998-4003 (2008).
32. B. Tawfik *et al.*, Synaptotagmin-7 places dense-core vesicles at the cell membrane to promote Munc13-2-and Ca2+-dependent priming. *Elife* **10** (2021).
33. J. H. Bai, W. C. Tucker, E. R. Chapman, PIP2 increases the speed of response of synaptotagmin and steers its membrane-penetration activity toward the plasma membrane. *Nature Structural & Molecular Biology* **11**, 36-44 (2004).
34. E. R. Chapman, A. F. Davis, Direct interaction of a Ca2+-binding loop of synaptotagmin with lipid bilayers. *Journal of Biological Chemistry* **273**, 13995-14001 (1998).

35. H. T. Tran, L. H. Anderson, J. D. Knight, Membrane-Binding Cooperativity and Coinsertion by C2AB Tandem Domains of Synaptotagmins 1 and 7. *Biophysical Journal* **116**, 1025-1036 (2019).
36. V. Shahin *et al.*, Synaptotagmin perturbs the structure of phospholipid bilayers. *Biochemistry* **47**, 2143-2152 (2008).
37. K. E. Ward, J. P. Ropa, E. Adu-Gyamfi, R. V. Stahelin, C2 domain membrane penetration by group IVA cytosolic phospholipase A(2) induces membrane curvature changes. *Journal of Lipid Research* **53**, 2656-2666 (2012).
38. S. Martens, M. M. Kozlov, H. T. McMahon, How synaptotagmin promotes membrane fusion. *Science* **316**, 1205-1208 (2007).
39. E. Hui, C. P. Johnson, J. Yao, F. M. Dunning, E. R. Chapman, Synaptotagmin-mediated bending of the target membrane is a critical step in Ca(2+)-regulated fusion. *Cell* **138**, 709-721 (2009).
40. K. C. Courtney *et al.*, The complexin C-terminal amphipathic helix stabilizes the fusion pore open state by sculpting membranes. *Nature Structural & Molecular Biology* **29**, 97-+ (2022).
41. E. Hui *et al.*, Mechanism and function of synaptotagmin-mediated membrane apposition. *Nature Structural & Molecular Biology* **18**, 813-821 (2011).
42. S. Martens, H. T. McMahon, Mechanisms of membrane fusion: disparate players and common principles. *Nature Reviews Molecular Cell Biology* **9**, 543-556 (2008).
43. J. Yao, S. E. Kwon, J. D. Gaffaney, F. M. Dunning, E. R. Chapman, Uncoupling the roles of synaptotagmin I during endo- and exocytosis of synaptic vesicles. *Nature neuroscience* **15**, 243-249 (2011).
44. J. S. Rhee *et al.*, Augmenting neurotransmitter release by enhancing the apparent Ca2+ affinity of synaptotagmin 1. *Proceedings of the National Academy of Sciences of the United States of America* **102**, 18664-18669 (2005).
45. E. F. Hui *et al.*, Mechanism and function of synaptotagmin-mediated membrane apposition. *Nature Structural & Molecular Biology* **18**, 813-U892 (2011).
46. H. K. Shapiro, R. L. Barchi, Alteration of synaptosomal plasma cholesterol content: Membrane physical properties and cation transport proteins. *Journal of Neurochemistry* **36**, 1813-1818 (1981).
47. V. Kiessling *et al.*, A molecular mechanism for calcium-mediated synaptotagmin-triggered exocytosis. *Nature Structural & Molecular Biology* **25**, 911-+ (2018).
48. M. Bendahmane *et al.*, The synaptotagmin C2B domain calcium-binding loops modulate the rate of fusion pore expansion. *Molecular Biology of the Cell* **29**, 834-845 (2018).
49. L. B. Li, I. Vorobyov, T. W. Allen, The Different Interactions of Lysine and Arginine Side Chains with Lipid Membranes. *Journal of Physical Chemistry B* **117**, 11906-11920 (2013).
50. D. S. Brandt, M. D. Coffman, J. J. Falke, J. D. Knight, Hydrophobic Contributions to the Membrane Docking of Synaptotagmin 7 C2A Domain: Mechanistic Contrast between Isoforms 1 and 7. *Biochemistry* **51**, 7654-7664 (2012).
51. D. Das, H. Bao, K. C. Courtney, L. Wu, E. R. Chapman, Resolving kinetic intermediates during the regulated assembly and disassembly of fusion pores. *Nat Commun* **11**, 231 (2020).
52. H. Bao *et al.*, Dynamics and number of trans-SNARE complexes determine nascent fusion pore properties. *Nature* **554**, 260-263 (2018).
53. Z. Wu *et al.*, The neuronal calcium sensor Synaptotagmin-1 and SNARE proteins cooperate to dilate fusion pores. *Elife* **10** (2021).
54. K. L. Lynch *et al.*, Synaptotagmin-1 Utilizes Membrane Bending and SNARE Binding to Drive Fusion Pore Expansion. *Molecular Biology of the Cell* **19**, 5093-5103 (2008).

55. L. Wu, K. C. Courtney, E. R. Chapman, Cholesterol stabilizes recombinant exocytic fusion pores by altering membrane bending rigidity. *Biophys J* **120**, 1367-1377 (2021).
56. M. Zick, W. Wickner, Improved reconstitution of yeast vacuole fusion with physiological SNARE concentrations reveals an asymmetric Rab(GTP) requirement. *Molecular Biology of the Cell* **27**, 2590-2597 (2016).
57. J. Yao, S. E. Kwon, J. D. Gaffaney, F. M. Dunning, E. R. Chapman, Uncoupling the roles of synaptotagmin I during endo- and exocytosis of synaptic vesicles. *Nature Neuroscience* **15**, 243-249 (2012).
58. M. S. Perin, V. A. Fried, G. A. Mignery, R. Jahn, T. C. Südhof, Phospholipid binding by a synaptic vesicle protein homologous to the regulatory region of protein kinase C. *Nature* **345**, 260-263 (1990).

## Author contributions

K.C.C., Q.C. and E.R.C. designed the study; K.C.C., T.M., Y.L., N.M. and D.D performed experiments and analyzed data; K.C.C. and E.R.C. wrote the manuscript; E.R.C. and Q.C provided funding.

## Acknowledgements

We are grateful to the other members of the Chapman lab and M.B. Jackson for providing critical feedback on this project. We also especially thank L. Wu and C. Greer for their editorial contributions. This work was supported by National Institutes of Health grants MH061876 and NS097362 (E.R.C.) and the National Science Foundation grant NSF-DMS1661900 (Q.C.) Computational resources from the Extreme Science and Engineering Discovery Environment (XSEDE(49)), which is supported by NSF grant number ACI-1548562, are greatly appreciated; part of the computational work was performed on the Shared Computing Cluster which is administered by Boston University's Research Computing Services (URL: www.bu.edu/tech/support/research/). E.R.C. is an Investigator of the Howard Hughes Medical Institute.

**Main figures**

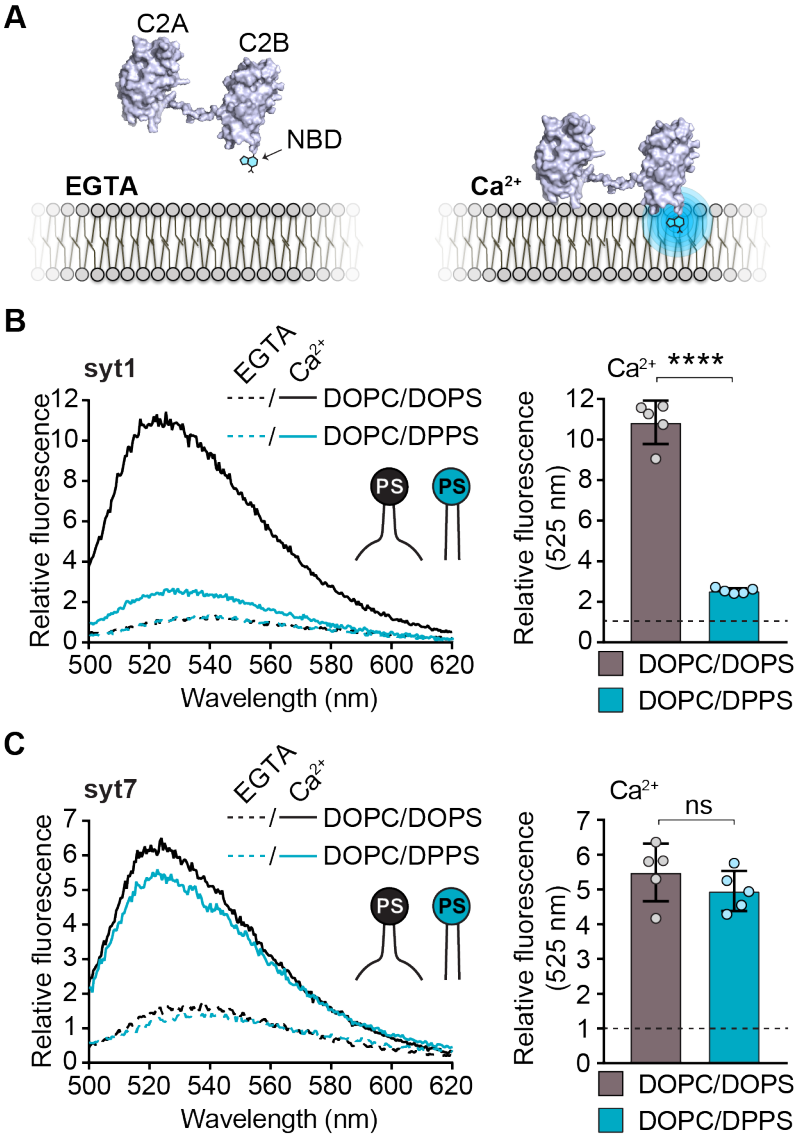


Figure 1 – **Syt1 cannot penetrate membranes that harbor saturated PS**

A) Illustration showing how an NBD labelled C2AB domain associates with a lipid bilayer in response to binding $Ca^{2+}$. After binding $Ca^{2+}$, the C2AB domain binds the membrane, thus inserting the NBD dye into the hydrophobic core of the bilayer, causing a blue shift and an increase in fluorescence intensity. B) Representative fluorescence emission spectra (*left panel*) of NBD labelled syt1, in the presence (solid lines) and absence (dotted lines) of $Ca^{2+}$, and liposomes composed of DOPC/DOPS (black) or DOPC/DPPS (blue). Quantification of NBD-syt1 C2AB fluorescence emission at 525 nm in the presence of $Ca^{2+}$ and liposomes composed of DOPC/DOPS (black) or DOPC/DPPS (blue), *right panel*. The data are normalized to the EGTA condition, shown as a horizontal black dotted line. C) Representative fluorescence emission spectra (*left panel*) and quantification (*right panel*) of NBD labelled syt7, under the

same conditions as *panel B*. Error bars represent standard error of the mean. **** represents $p<0.0001$ and ns represents a non-significant difference between conditions.

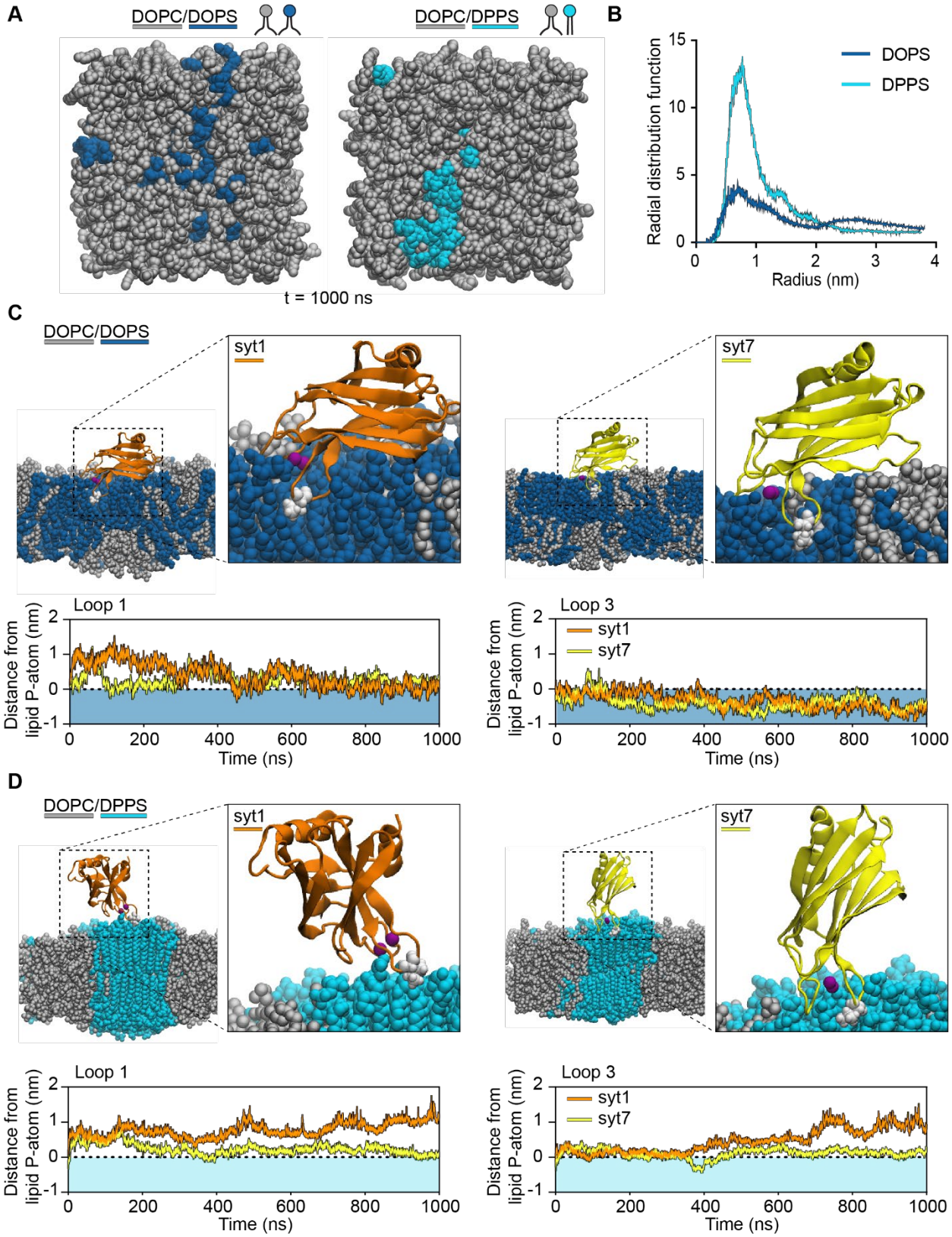
A
DOPC/DOPS
DOPC/DPPS
t = 1000 ns
B
Radial distribution function
Radius (nm)
DOPS
DPPS
C
DOPC/DOPS
syt1
syt7
Loop 1
Loop 3
Distance from lipid P-atom (nm)
Time (ns)
D
DOPC/DPPS
syt1
syt7
Loop 1
Loop 3
Distance from lipid P-atom (nm)
Time (ns)

Figure 2 – **The C2B domain of syt7, but not syt1, penetrates lipid bilayers that harbor DPPS**

A) End-point (450 ns) MD simulations of lipid bilayers composed of DOPC/DOPS or DOPC/DPPS. The PS lipids were initially placed as a cluster in the center of the membrane (see Figure S2 for the starting images) and then allowed to freely diffuse over time. B) Radial distribution functions comparing the clustering behavior of DOPS and DPPS in the lipid bilayer at the end of the simulation shown in *panel A*. C) End point (1000 ns) MD simulations snapshots showing syt1 (orange) and syt7 (yellow) C2B domains interacting with lipid bilayers composed of DOPC/DOPS. Quantification of loop 1 and loop 3 depth from syt1 and syt7 are shown in the lower panels. The loop depth is shown relative to the lipid phosphate group. D) End point (1000 ns) MD simulations snapshots showing syt1 (orange) and syt7 (yellow) C2B domains interacting with lipid bilayers composed of DOPC/DPPS. Quantification of loop 1 and loop 3 depth from syt1 and syt7 are shown in the lower panels. The loop depth is shown relative to the lipid phosphate group.

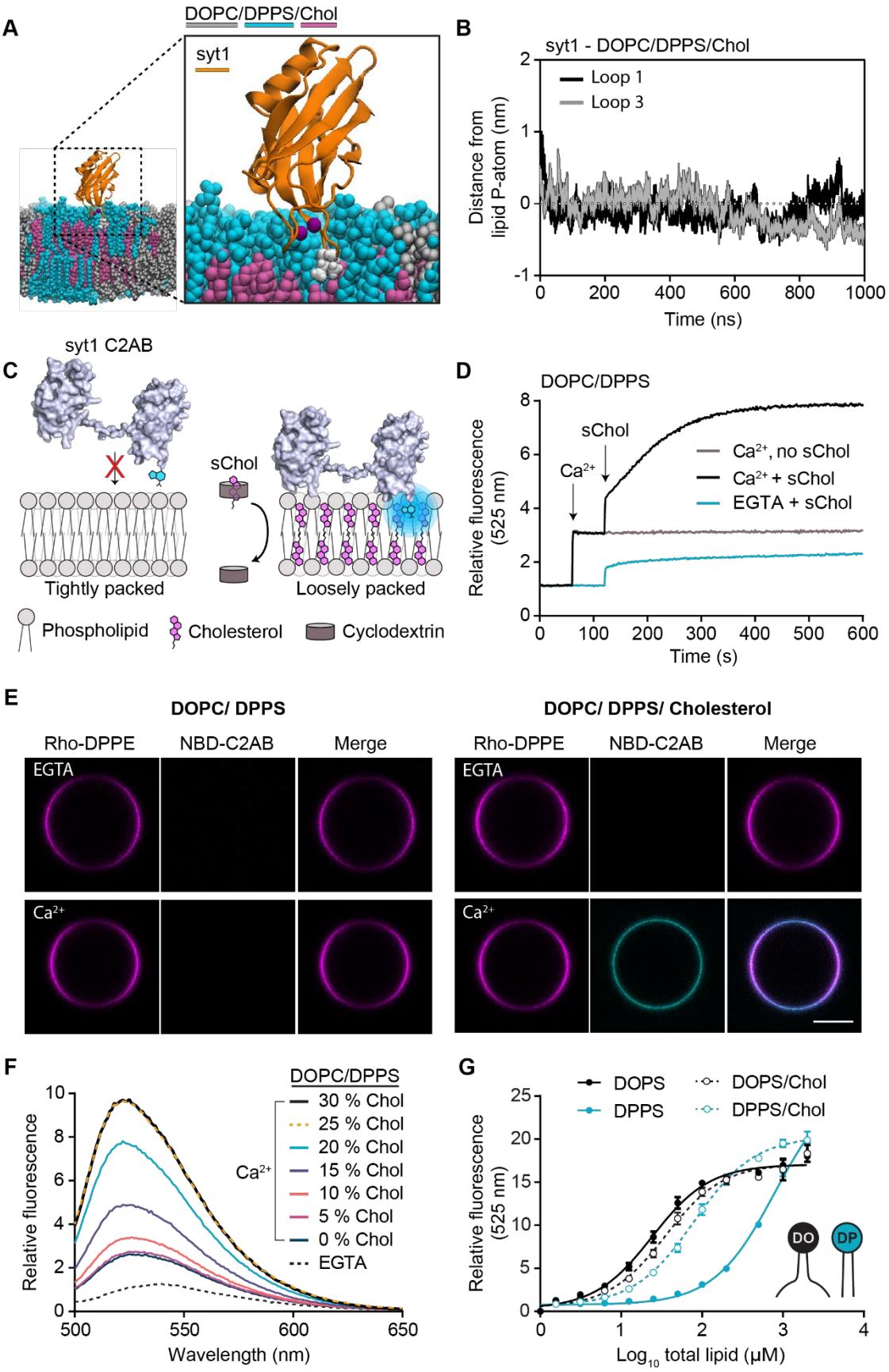
A
DOPC/DPPS/Chol
syt1
B
syt1 - DOPC/DPPS/Chol
Loop 1
Loop 3
Distance from lipid P-atom (nm)
Time (ns)
C
syt1 C2AB
sChol
Tightly packed
Loosely packed
Phospholipid
Cholesterol
Cyclodextrin
D
DOPC/DPPS
sChol
Ca2+
Ca2+, no sChol
Ca2+ + sChol
EGTA + sChol
Relative fluorescence (525 nm)
Time (s)
E
DOPC/ DPPS
DOPC/ DPPS/ Cholesterol
Rho-DPPE
NBD-C2AB
Merge
EGTA
Ca2+
F
DOPC/DPPS
30 % Chol
25 % Chol
20 % Chol
15 % Chol
10 % Chol
5 % Chol
0 % Chol
EGTA
Ca2+
Relative fluorescence
Wavelength (nm)
G
DOPS
DPPS
DOPS/Chol
DPPS/Chol
DO
DP
Relative fluorescence (525 nm)
Log10 total lipid (μM)

Figure 3 – **Cholesterol enables syt1 to penetrate into bilayers containing DPPS**
A) MD simulations snapshot after 1000ns of a syt1 C2B domain (shown in orange) interacting with a phospholipid bilayer composed of DOPC/DPPS/cholesterol. DOPC is shown in grey, DPPS in cyan and cholesterol shown in magenta. Residue I367 on loop 3 of syt1 is emphasized in white and the bound $Ca^{2+}$ ions are shown in purple. B) Quantification of the penetration depth of loops 1 and 3 from syt1 C2B domain throughout the 1000 ns simulation. The loop depth is normalized relative to the position of the lipid phosphate group, indicated by a horizontal dotted line. C) An illustration depicting experimental C2 domain membrane penetration assay with the addition of a cholesterol-cyclodextrin complex, known as soluble cholesterol (sChol). In the absence of cholesterol, syt1 C2AB cannot penetration into the bilayer containing DPPS. When sChol is applied, cholesterol is donated into the DPPS bilayer, which enables syt1 C2AB to bind and penetrate into the membrane. D) Representative time course examining NBD-labelled syt1 C2AB fluorescence in the presence of DOPC/DPPS (80:20) under the indicated conditions. E) Fluorescence microscopy imaging of giant unilamellar vesicles, labelled with 0.1% rhodamine-DPPE, (magenta) and NBD-labelled syt1 C2AB (cyan) in the presence and absence of $Ca^{2+}$. The vesicles were composed of DOPC/DPPS (80:20) or DOPC/DPPS/cholesterol (56:14:30). The appearance of fluorescence signal in the NBD-C2AB channel indicates binding to the vesicles. Note: the non-uniform fluorescence in the Rho-DPPE channel is an optical aberration and is not indicative of lipid phase separation. The scale bar indicates 5 µm. F) Representative fluorescence spectra of NBD-labelled syt1 C2AB with various 100 nm liposome populations composed of DOPC/DPPS and increasing cholesterol. G) Quantification of a liposome titration in the presence of NBD-labelled syt1 C2AB. The protein concentration was fixed a 250 nM and the fluorescence at 525 nm was monitored as the concentration of lipid increased from 0-500 µM. Error bars represent standard error of the mean from triplicate experiments performed on separate days with fresh materials.

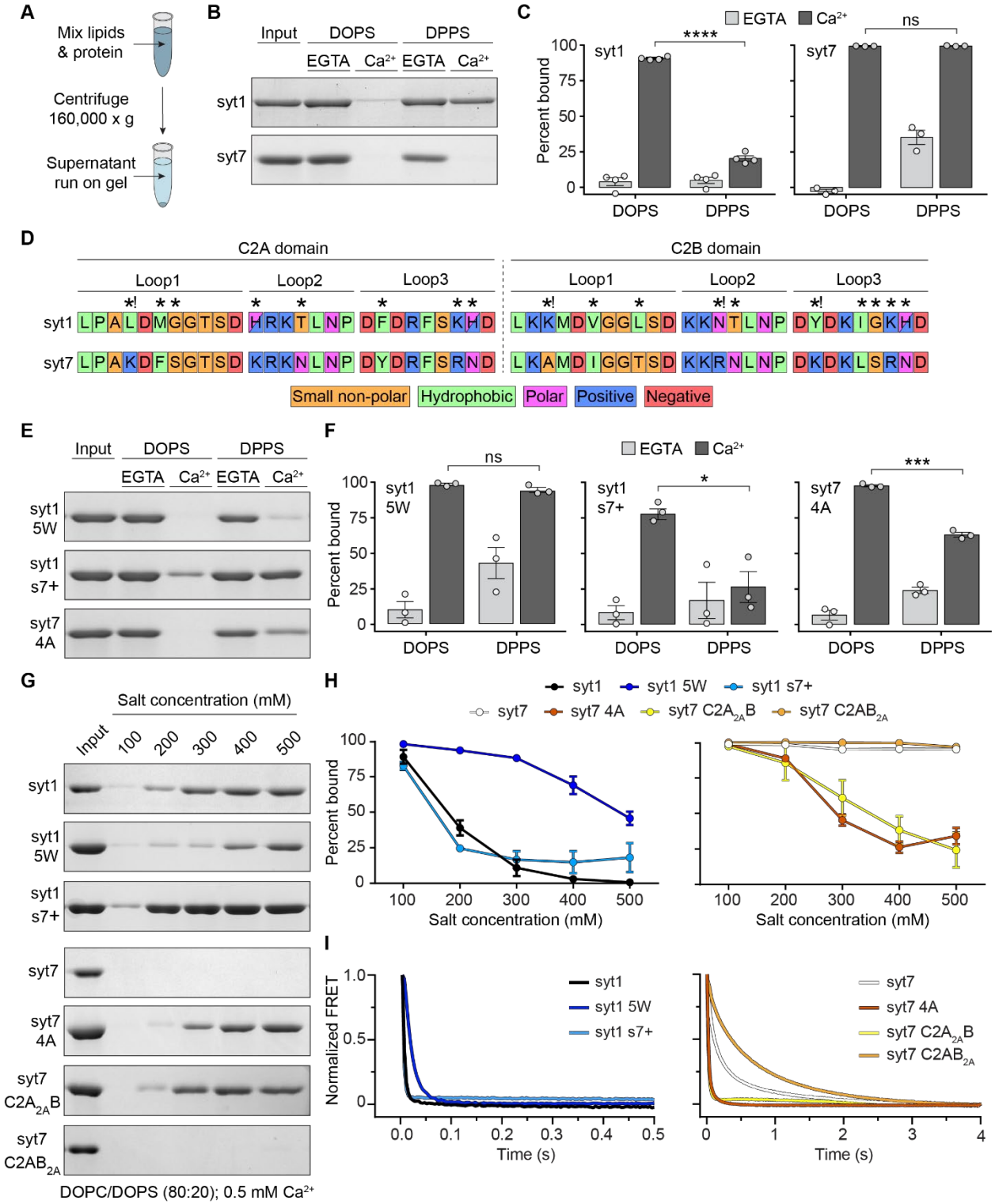


Figure 4 – **Hydrophobic interactions dominate C2AB-membrane binding**

A) Illustration of the liposome-protein co-sedimentation assay. Proteins and liposomes are mixed, followed by sedimentation of the liposomes; the supernatant is subjected to SDS-PAGE

to assay for protein depletion. B) Representative Coomassie stained SDS-PAGE gels of syt1 and syt7 co-sedimentation samples, in the presence and absence of $Ca^{2+}$, using liposomes composed of DOPC/DOPS or DOPC/DPPS. Throughout the figure, “Input” refers to the protein-only control sample. C) Quantification of the replicated syt1 and syt7 co-sedimentation assays comparing binding to DOPS and DPPS containing liposomes. D) Amino acid sequences of the penetration loops of syt1 and syt7 C2A and C2B domains. Unique residues at comparable positions between the two sequences are indicated by an asterisk (*). Unique residues with a differences in charge are indicated by asterisk and exclamation point (*!). E) Representative Coomassie stained SDS-PAGE gels of mutant syt1 and syt7 co-sedimentation samples, in the presence and absence of $Ca^{2+}$, and liposomes composed of DOPC/DOPS or DOPC/DPPS. F) Quantification of the mutant syt1 and syt7 co-sedimentation assays comparing binding to DOPS- and DPPS-bearing liposomes. G) Representative Coomassie stained SDS-PAGE gels of WT and mutant syt1 and syt7 co-sedimentation samples containing between 100 and 500 mM salt. H) Quantification of the replicated WT and mutant syt1 and syt7 co-sedimentation samples containing between 100 and 500 mM salt. I) Disassembly of $Ca^{2+}$-dependent WT and mutant syt1 and syt7 complexes with liposomes, measured by stopped flow rapid mixing with the $Ca^{2+}$ chelator, EGTA. Error bars represent standard error of the mean. Within the bar graphs, ****, ***, * and ns represents $p<0.0001$, $p<0.001$, $p<0.5$ and a non-significant difference, respectively.

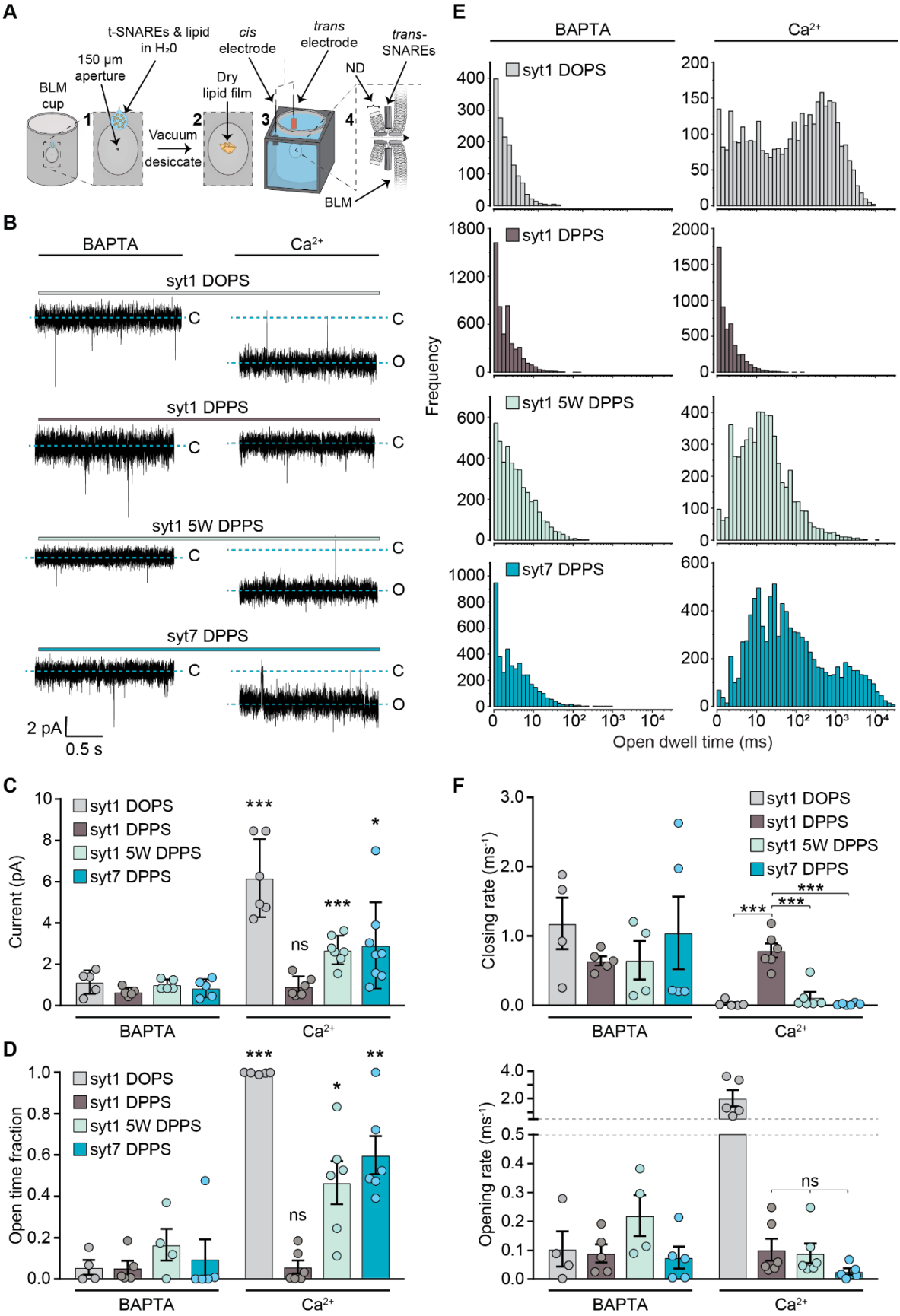
A
t-SNAREs & lipid in H₂0
150 µm aperture
BLM cup
1
Vacuum
desiccate
2
Dry lipid film
cis electrode
trans electrode
3
ND
4
trans-SNAREs
BLM
B
BAPTA
Ca2+
syt1 DOPS
syt1 DPPS
syt1 5W DPPS
syt7 DPPS
C
O
2 pA
0.5 s
E
Frequency
Open dwell time (ms)
C
Current (pA)
D
Open time fraction
F
Closing rate (ms-1)
Opening rate (ms-1)
ns

Figure 5 – **Membrane penetration is required for syts to dilate and stabilize the open state of fusion pores**

A) Illustration of the modified BLM protocol using lipid desiccation, which facilitated the formation of planar lipid bilayers containing DPPS. B) Representative raw traces of syt1, syt1 5W and syt7 ND-BLM recordings. ND3-syt1 experiments were performed with 20% DOPS in the BLM as a positive control for the effect of $Ca^{2+}$ on fusion pore properties The remaining traces were performed with 20% DPPS in the BLM, in 0.5 mM BAPTA or 0.5 mM free $Ca^{2+}$. C) Quantification of the current passing through ND-BLM fusion pores under the indicated conditions. D) Quantification of the fraction of time that ND-BLM fusion pores remained in the open state under the indicated conditions. E) Open dwell time distributions from the indicated ND-BLM fusion pore conditions. The data from each replicated condition are pooled. F) Opening and closing rates of ND-BLM fusion pores derived from the indicated closed and open dwell time analyses, respectively. Error bars represent standard error of the mean. Within the bar graphs, ****, ***, **, * and ns represents $p<0.0001$, $p<0.001$, $p<0.01$, $p<0.05$ and a non-significant difference, respectively.

**Supplemental Figures**

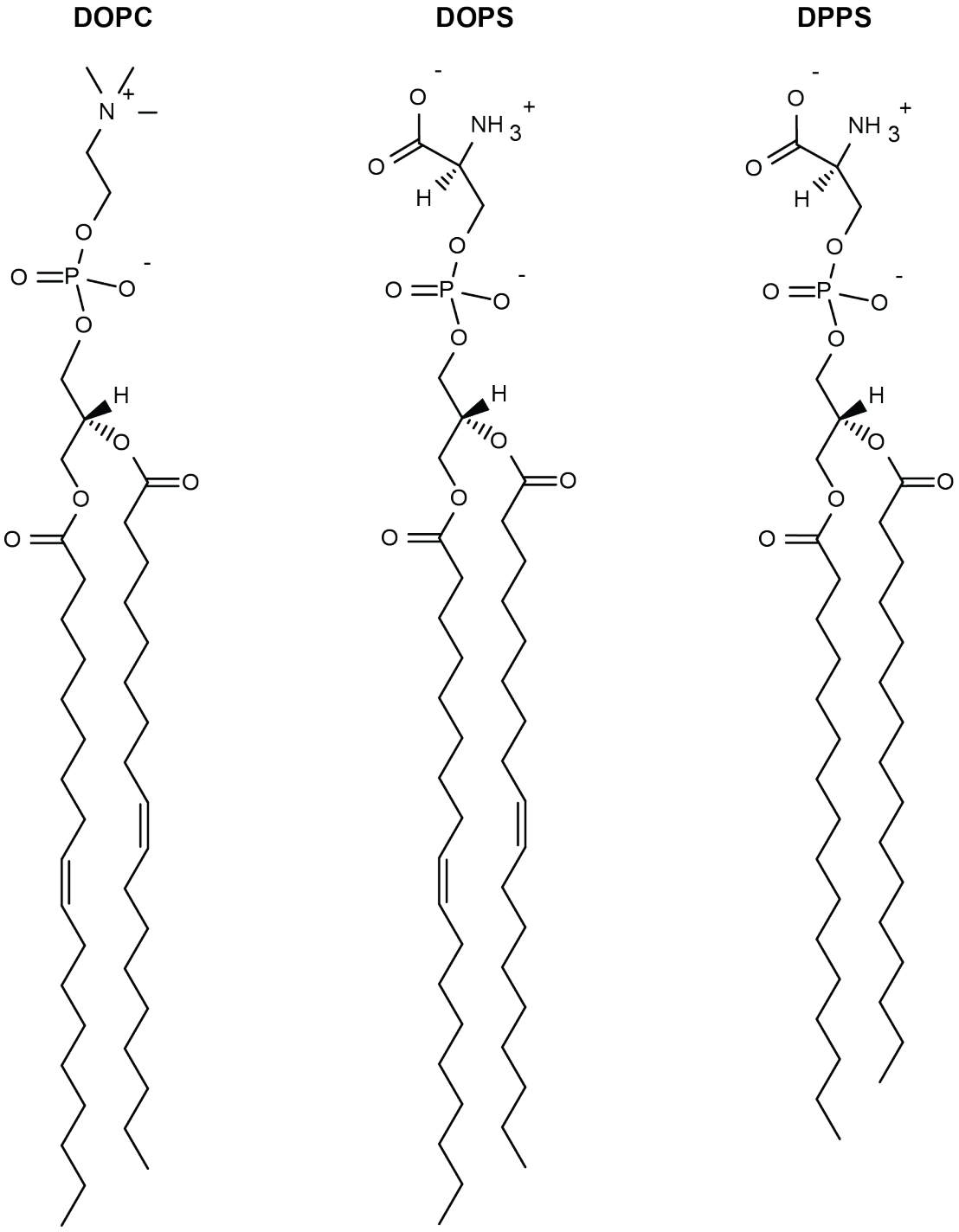


Figure S1 – **Phospholipid structures**
Chemical structures of the phospholipids used in this study

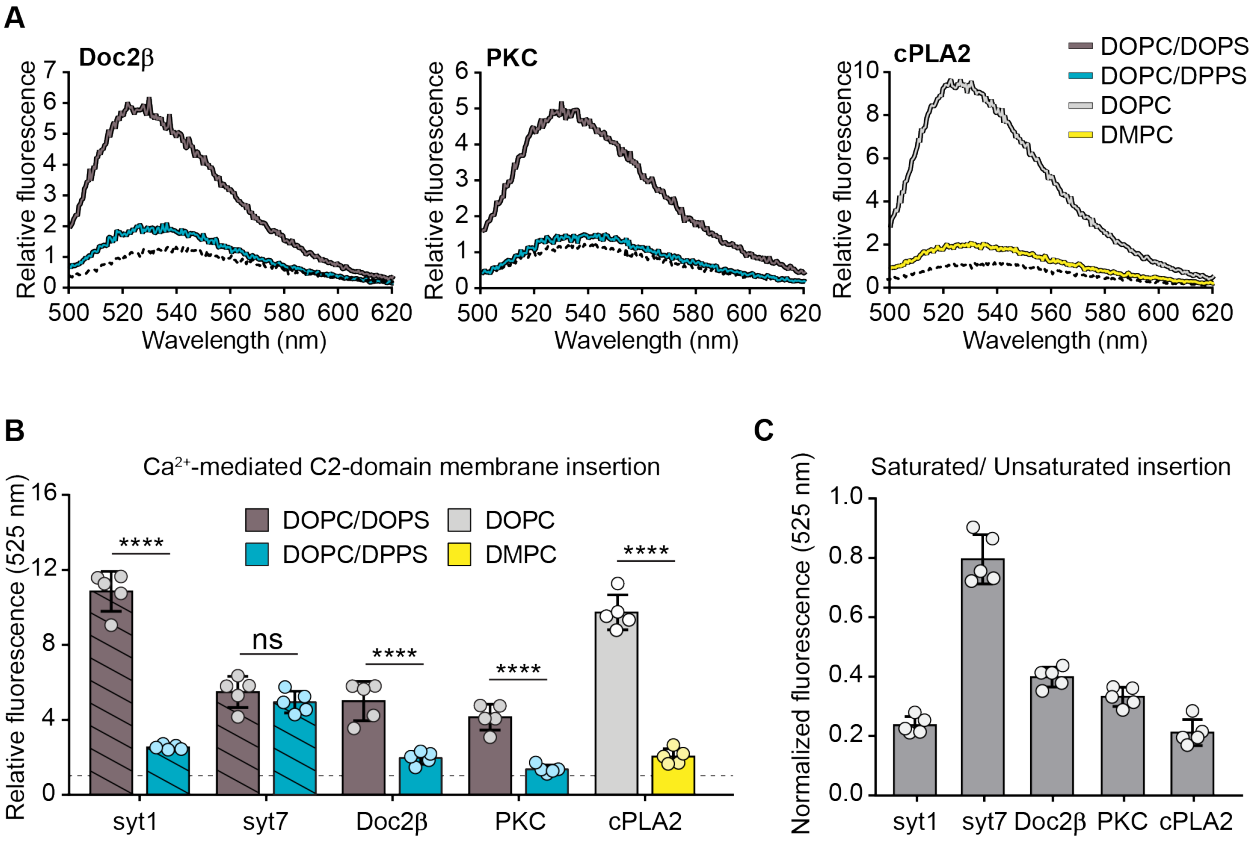


Figure S2 – **Doc2β, PKC and cPLA2 fail to penetrate into bilayers with saturated acyl chains**

A) Representative fluorescence spectra from NBD labeled Doc2β, PKC and cPLA2 in the presence and absence of $Ca^{2+}$. The NBD fluorescence in EGTA is represented as a black dotted line. The Doc2β and PKC experiment were performed with liposomes composed of DOPC/DOPS or DOPC/DPPS (80:20); the cPLA2 experiments were performed with liposomes composed of DOPC or DMPC, due to the inherent lack of PS binding specificity. B) Quantification of replicated experiments described in *panel A.* Replicates were performed on separate days with fresh lipid samples. The fluorescence intensity at 525 nm was extracted from each spectrum and plotted. The horizontal dotted line represents the normalized fluorescence intensity the EGTA conditions. The syt1 and syt7 data are reproduced from Figure 1 for comparison and emphasized with diagonal lines. C) Normalized NBD fluorescent intensities at 525 nm from data represented in *panel B*. The fluorescence in the saturated acyl chain conditions were divided by the condition containing all unsaturated acyl chains. Error bars represent standard error of the mean. Within the bar graph, **** and ns represents $p<0.0001$ and a non-significant difference, respectively.

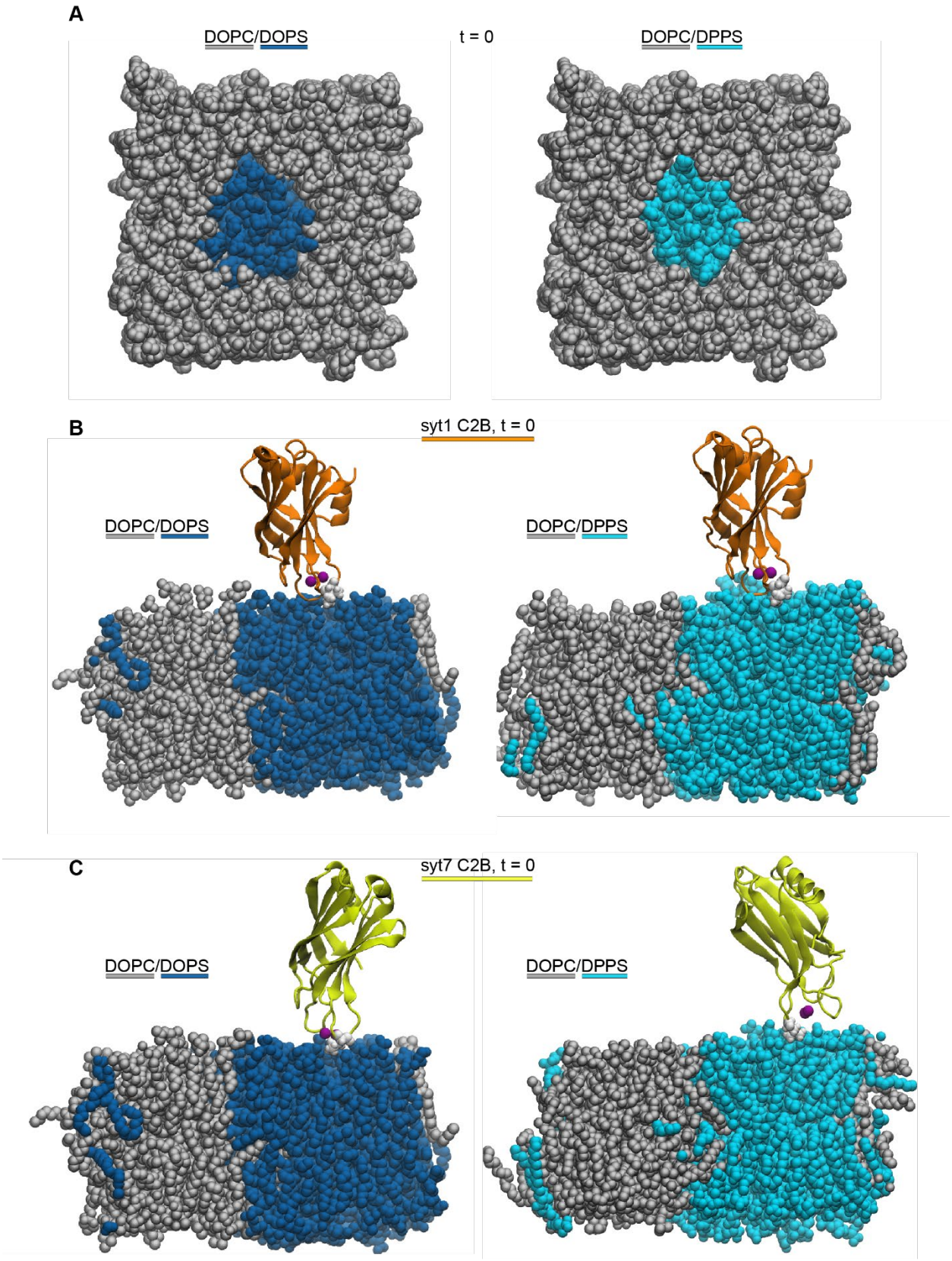
A
DOPC/DOPS
t = 0
DOPC/DPPS
B
syt1 C2B, t = 0
DOPC/DOPS
DOPC/DPPS
C
syt7 C2B, t = 0
DOPC/DOPS
DOPC/DPPS

Figure S3 – **Initial configurations of MD simulations**
A) Time zero snapshots of MD simulations that examine the clustering behavior of DOPS (*left*) and DPPS (*right*) among DOPC lipids (grey). B) Time zero snapshots of MD simulations comparing penetration of syt1 C2B (shown in orange) domain into bilayers containing 20% DOPS (*left*) or DPPS (*right*). C) Time zero snapshots of MD simulations comparing penetration of syt7 C2B domain (shown in yellow) into bilayers containing 20% DOPS (*left*) or DPPS. Corresponding end-point snapshots from all panels are found in Figure 2.

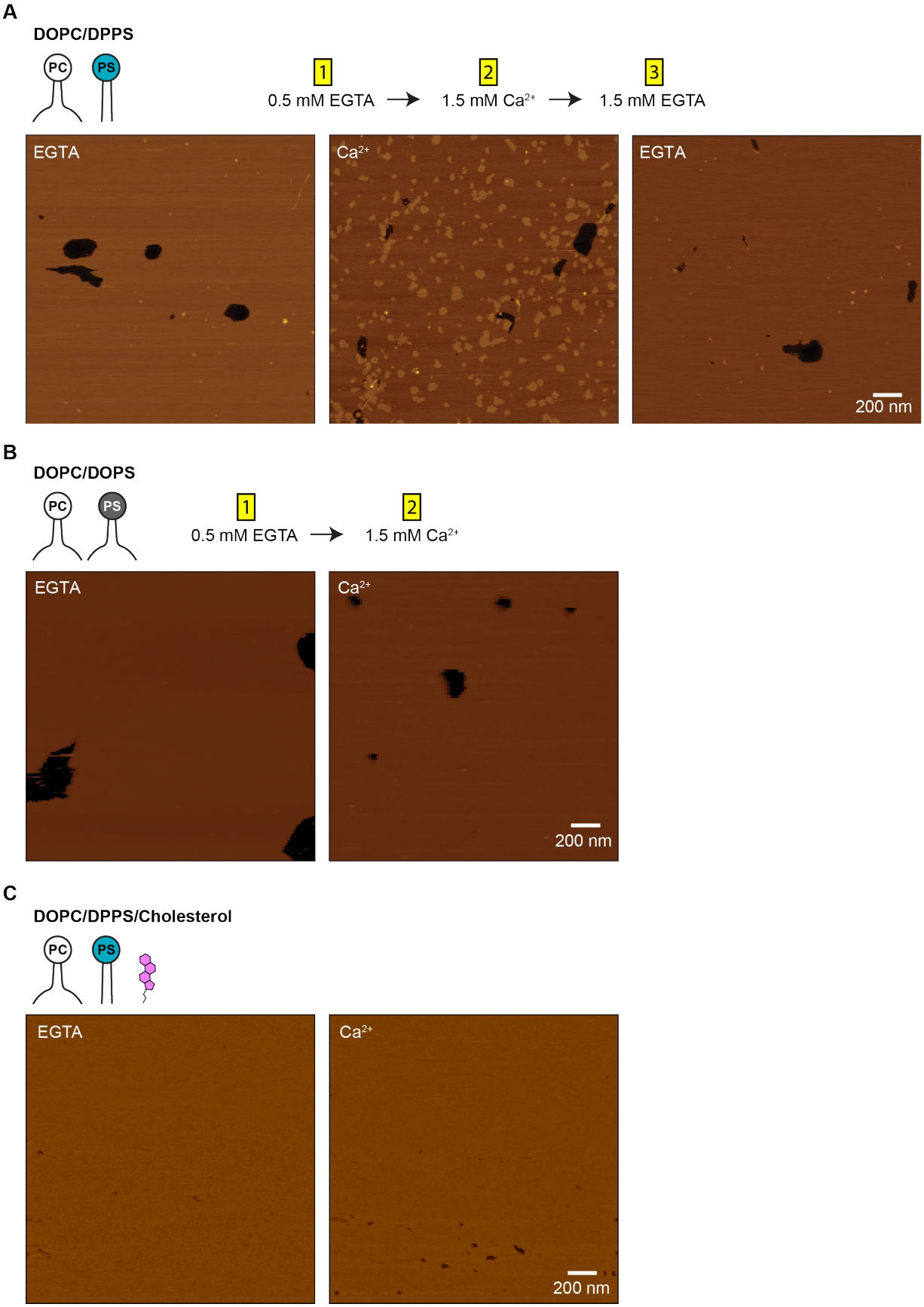
A
DOPC/DPPS
PC
PS
1
0.5 mM EGTA
2
1.5 mM Ca2+
3
1.5 mM EGTA
EGTA
Ca2+
EGTA
200 nm
B
DOPC/DOPS
PC
PS
1
0.5 mM EGTA
2
1.5 mM Ca2+
EGTA
Ca2+
200 nm
C
DOPC/DPPS/Cholesterol
PC
PS
EGTA
Ca2+
200 nm

Figure S4 – **$Ca^{2+}$ causes DPPS clustering in lipid bilayers**
A) AFM imaging of supported lipid bilayers on mica composed of DOPC/DPPS (80:20) with and without $Ca^{2+}$. B) AFM imaging of supported lipid bilayers on mica composed of DOPC/DOPS (80:20) with and without $Ca^{2+}$. C) AFM imaging of supported lipid bilayers on mica composed of DOPC/DPPS/cholesterol (56:14:30) with and without $Ca^{2+}$.

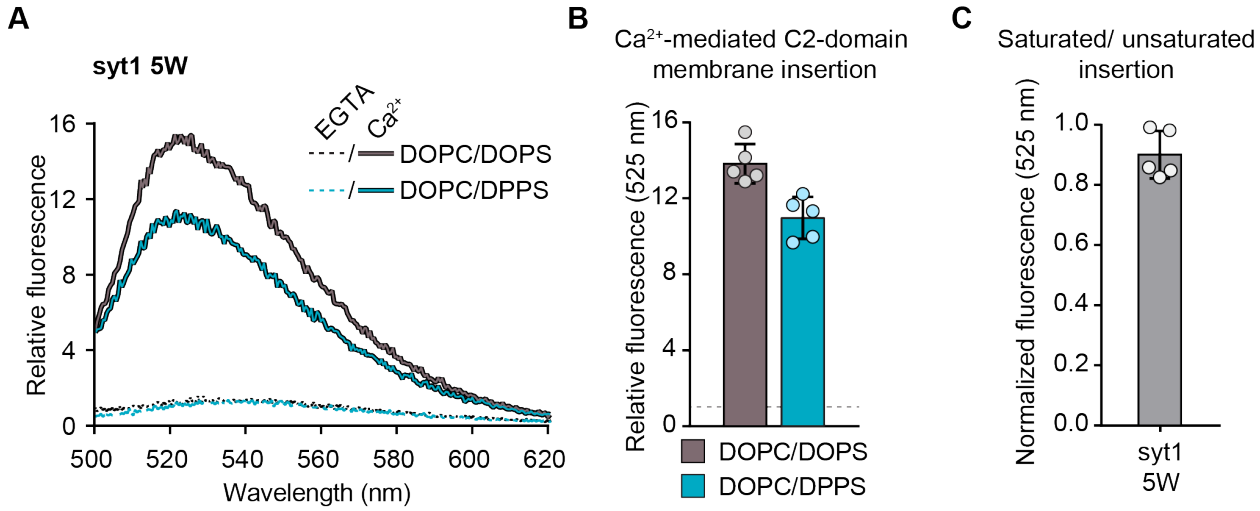


Figure S5 – **Increased hydrophobicity in the penetration loops enables syt1 C2AB to penetration bilayers that harbor DPPS**

A) Representative fluorescence spectra of NBD-labelled syt1 5W C2AB in 0.2 mM EGTA (dotted lines) or 0.5 mM free $Ca^{2+}$ (solid lines) and with liposomes composed of DOPC/DOPS or DOPC/DPPS (80:20). B) Quantification of replicated experiments depicted in *panel A*. The normalized fluorescence intensity at 525 nm in $Ca^{2+}$ is shown relative to the EGTA condition. C) Normalized NBD fluorescent intensity at 525 nm from data represented in *panel B*. The fluorescence in the saturated acyl chain conditions were divided by the condition containing all unsaturated acyl chains.

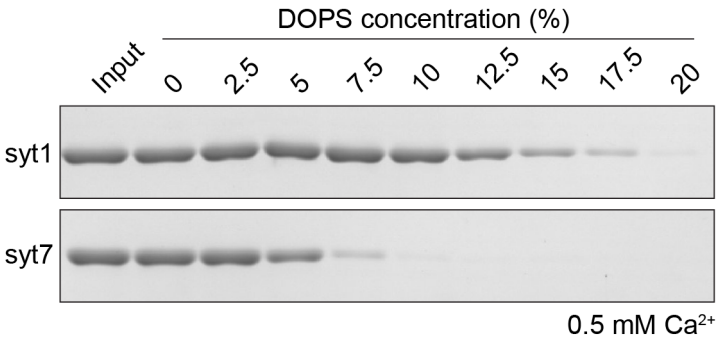


Figure S6 – **Syt7 displays higher affinity for PS-bearing liposomes than syt1**
Representative Coomassie stained SDS-PAGE gel of a co-sedimentation assay (described in Figure 3A) with syt1 and syt7 C2AB domains in the presence of $Ca^{2+}$ and liposomes with increasing mole fractions of PS. Depletion of protein from the samples indicates binding to liposomes. Input refers to the protein-only control sample.

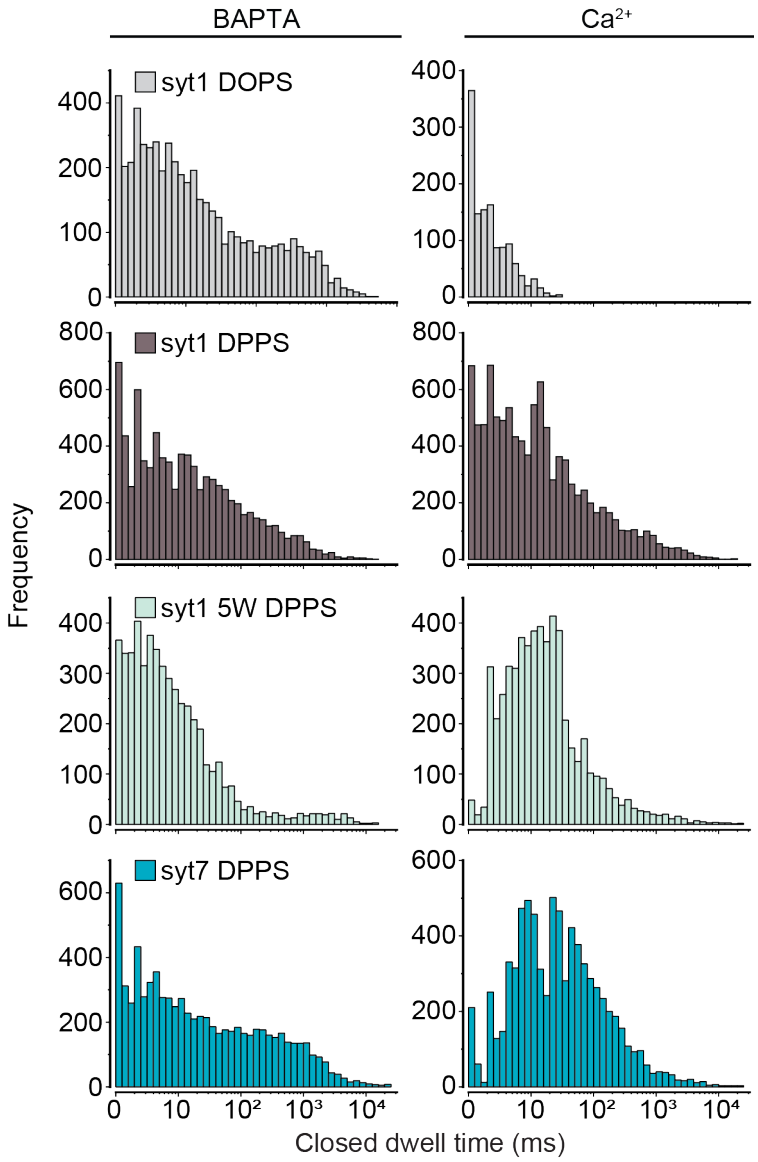


Figure S7 – **In the presence of $Ca^{2+}$ and $ND_3$-syt1 5W or $ND_3$-syt7, SNARE-mediated fusion pore exhibit long closed dwell times when the BLM harbors DOPC/DPPS**
Closed dwell time distributions generated and pooled from each of the indicated ND-BLM conditions, in 0.5 mM BAPTA or 0.5 mM free $Ca^{2+}$.

## Methods

### Protein purification

Recombinant proteins were produced in *E. coli* (BL21) and purified using Ni-NTA or TALON metal affinity agarose resin as previously described (40). Syb2, FL-syt1, syt1 C2AB (residues 96-421; I367C), FL-syt1 5W (M173W, F231W, F234W V304W, Y364W, I367C), syt1 5W C2AB, cPLA2 (Y96C), PKC (L249C), FL-syt7, syt7 (L361C) and Doc2β (G361C) were purified as SUMO fusion proteins. With the exception of cPLA2 and PKC, the SUMO domain was cleaved from the protein of interest by incubation with 0.5 μM SENP2 protease overnight at 4 ºC. cPLA2, PKC, MSP1E3D1 and the SNAP-25B/syntaxin1a heterodimer were eluted from the Ni-NTA resin by 500 mM imidazole, followed by running the sample through a PD-10 desalting column to remove the imidazole. Proteins that contained a transmembrane domain were purified with the addition of 0.9% CHAPS in the buffers. The protein concentrations were determined by Coomassie stained SDS-PAGE and compared with a range of BSA standards.

### NBD labeling

The cPLA2 and PKC C2 domains were engineered to harbor a single cysteine residue in loop 3 of their single C2 domains, while syt1, syt1 5W, syt7 and Doc2β C2AB domains had a single cysteine in loop 3 of their C2B domains. The mutations for the single cysteine variants are listed above in the protein purification section. To conjugate NBD to the cysteine thiol group, 50 μM of each protein was incubated with at least 10-fold excess iodoacetamide-NBD overnight at 4 ℃, followed by removal of free dye using a PD-10 desalting column. Protein labeling efficiency (>80 %) was calculated using the Beers-Lambert law ($A = \varepsilon cl$) with the NBD extinction coefficient of 25000 $M^{-1}$ $cm^{-1}$ at 480 nm to determine NBD content, and this value was compared to the protein concentration.

### Preparation of unilamellar vesicles

Large unilamellar vesicles (LUVs) were prepared by pipetting chloroform suspended lipids into a glass tube, followed by drying the sample under a stream of nitrogen gas.

After formation of a thin lipid film, the sample was then placed in a lyophilizer for at least 60 minutes to remove residual organic solvent. The lipids were hydrated with 25 mM HEPES, 100 KCl pH 7.4 and placed at 50 ºC to aid in resuspension, followed by vortexing to generate multilamellar vesicles. The sample was then repeatedly passed through a 100 nm filter using a mini extruder system (Avanti Polar Lipids) to result in uniform LUVs.

Giant unilamellar vesicles (GUVs) were prepared by electroformation from a lipid film on indium tin oxide (ITO) coated glass slides, as previously described (59). This procedure was carried out as follows: stock solutions of lipids (1 mM) with various acyl chain structures were prepared in chloroform composed of PC/PS (80:20) or PC/PS/cholesterol (56:14:30), plus 0.1 % rhodamine-DOPE. Fifteen µl of the stock lipids were deposited dropwise onto three regions of two ITO slides under a stream of nitrogen gas. A greased PTFE o-ring was then placed around each of the 3 regions of deposited lipid and the o-rings were filled with 1 mM HEPES, 200 mM sucrose (pH 7.4) solution. The second ITO slide was placed on top to seal the o-rings between the two ITO slides. To initiate electroformation, the ITO slides were connected to a function generator and subjected to an alternating sine wave set to 10 Hz and 3 $V_{pp}$ at 50 ℃. After 2 hours, the frequency was changed to 0.5 Hz for 5 - 10 minutes to stimulate the release of vesicles from the glass surface. After electroformation, the ITO slides were separated and the GUV solution was recovered from within the o-rings. The collected GUVs were then washed with 20 mM HEPES, 100 mM KCl (pH 7.4) and gently filtered to purify GUVs greater than 3 µm in diameter. Finally, the GUVs were transferred to BSA-treated glass bottom 96 well plate and imaged with a Zeiss 880 airyscan microscope using a 63x objective.

**Co-sedimentation assay**

One hundred nm LUVs (0.5 mM) composed of DOPC/DOPS or DOPC/DPPS (80:20) were mixed with 2.5 µM of the indicated C2AB proteins in 0.2 mM EGTA or 0.5 mM free $Ca^{2+}$. The LUVs, or protein-LUV complexes, were then pelleted by ultracentrifugation at 65,000 RPM in a TLA-100 rotor (Beckman). The unbound fraction C2AB in the supernatants was quantified by densitometry analysis of Coomassie blue stained SDS-

PAGE gels. For experiments with increasing salt, the samples received progressive increases in NaCl.

**Atomic force microscopy**

Supported lipid bilayers composed of DOPC/DOPS, DOPC/DPPS (80:20) or DOPC/DPPS/Cholesterol (56:14:30) were prepared by first generating 1 mM LUVs, as described above, followed by incubating a 10-fold diluted sample with freshly cleaved mica discs in a liquid cell. The AFM imaging of the supported lipid bilayers was performed using an Agilent 5500 Scanning Probe Microscope, as previously described (60).

**Molecular dynamics simulations**

The syt1 C2B protein crystal structure was taken from the PDB database (PDB ID 1K5W). The lipid models were generated using CHARMM-GUI software (61). The CHARMM36 forcefield (62) was used to model all the components of the system. To check the stability of PS clusters, we first built a cylindrical cluster containing 32 DPPS or DOPS lipids. This PS cluster was then inserted into the center of a DOPC bilayer (**Figure S3A**). The lipid bilayer was then solvated using TIP3P water box of (~9.4 × 9.4 × 8.0 $nm^3$) and 32 $Ca^{2+}$ and 32 $Cl^-$ ions were added to the system. The solvated system was first energy-minimized using conjugate gradient method to remove any bad contacts between the solvent and solute atoms. This step was followed by a short NVT simulation in which phosphorous atoms of the lipid heads were restrained. The NVT equilibrated system was then subject to restraint-free NPT equilibration at the atmospheric pressure and room temperature. The temperature and pressure of the system were controlled using Nose-Hoover thermostat with a time constant of 1 ps and Parrinello-Rahman barostat with a time constant of 5 ps, respectively. The covalent bonds involving light hydrogen atoms were constrained using LINCS algorithm to enable the simulation time step of 2 fs. Periodic boundary conditions were enforced in all three directions and the long-range electrostatic interactions were calculated using particle-mesh-Ewald (PME) method. The short-ranged van der Waals forces was smoothly decayed to zero in the range of 1.0 to

1.2 nm using a switching function. All simulations were carried out using the Gromacs suite of programs (63).

**Stopped-flow rapid mixing**

Rapid mixing was performed using a SX-18.MV stopped-flow spectrometer (Applied Photophysics). Samples constituting protein (4 μM), liposomes (1 mM lipids composed of 70% DOPC, 25% DOPS, and 5% dansyl-PE), and $CaCl_2$ (250 μM) were allowed to rapidly mix with an equal volume of EGTA (2 mM) at room temperature (23° C). Before mixing, the samples were allowed to equilibrate for 5 min in their respective syringes of the spectrometer. Endogenous protein tryptophan residues were excited at 295 nm and the emission of the dansyl, due to FRET, was monitored via using a 470 nm long-pass filter (KV470, Schott). The reaction volume was set to 120 μl in the stopped-flow instrument. Using Applied Photophysics Pro-Data SX software, the average traces were fitted with either single or double exponential functions and the kinetic values were selected based on the minimum chi-square value of the fitted curve. A few initial data points (within 1 ms) were omitted from the fit to account for the dead-time of the instrument. The experiments were done in biological as well as technical triplicates.

**Nanodisc-black lipid membrane electrophysiology**

Reconstitution of three copies of syb2 with three copies of syt1, syt1 5W or syt7 into nanodiscs and t-SNARE SUVs were performed as previously described (40). In contrast to previous nanodisc-black lipid membrane (ND-BLM) experiments (40), planar lipid bilayers were formed by drying lipids that were resuspended in water, rather than decane. See Figure 5A for an illustration of this procedure. This method was developed as DPPS is not soluble in the typical solvent used to form the bilayers, decane, used in classical approaches. Throughout this manuscript, the same planar lipid bilayer formation strategy was used, regardless of lipid mixture to ensure that samples can be directly compared. Bilayers were formed by resuspending 30 mM of either DOPC/DOPS or DOPC/DPPS in pure water. Five μl of the lipids were mixed with 1 μl t-SNARE reconstituted SUVs (~ 400 μM lipids, 400 nM protein) and pipetted as a droplet over the aperture in the bilayer cup. The bilayer cup, with the lipid droplet is then place

horizontally in a vacuum desiccator for 60 minutes to evaporate the water and form a lipid film across the aperture. As soon as the lipid is dried, the bilayer cup is placed in the bilayer chamber and 25 mM HEPES, 10 mM KCl pH 7.4 buffer is added to the *trans* chamber. To break through the dried lipid, and 'unplug' the cup aperture, press firmly on top of the cup to force a small volume of buffer through the aperture, followed by filling the *cis* chamber with 25 mM HEPES, 100 mM KCl. Next, use a fine tipped paint brush, dipped in decane, to re-seal the cup aperture and form the planar lipid bilayer. Note that while DPPS is not soluble in pure decane, when the lipids are in the presence of water, this mixture of polar and non-polar solutions facilitates the formation of a bilayer harboring DPPS. After the bilayer is formed, a *cis* chamber buffer exchange is performed to remove free-floating lipid and t-SNAREs. Subsequent ND-BLM experiments are conducted and analyzed as previously described (40).

## Methods references


59. L. Liu *et al.*, Beyond Amphiphilic Balance: Changing Subunit Stereochemistry Alters the Pore-Forming Activity of Nylon-3 Polymers. *J Am Chem Soc* (2021).
60. K. C. Courtney *et al.*, Synaptotagmin 1 oligomerization via the juxtamembrane linker regulates spontaneous and evoked neurotransmitter release. *Proceedings of the National Academy of Sciences* **118**, e2113859118 (2021).
61. S. Jo, T. Kim, V. G. Iyer, W. Im, Software news and updates - CHARNIM-GUI: A web-based grraphical user interface for CHARMM. *Journal of Computational Chemistry* **29**, 1859-1865 (2008).
62. J. B. Klauda *et al.*, Update of the CHARMM All-Atom Additive Force Field for Lipids: Validation on Six Lipid Types. *Journal of Physical Chemistry B* **114**, 7830-7843 (2010).
63. M. J. Abraham *et al.*, GROMACS: High performance molecular simulations through multi-level parallelism from laptops to supercomputers. *SoftwareX* **1-2**, 19-25 (2015).